Philip Hofmann

Surface Physics

An Introduction

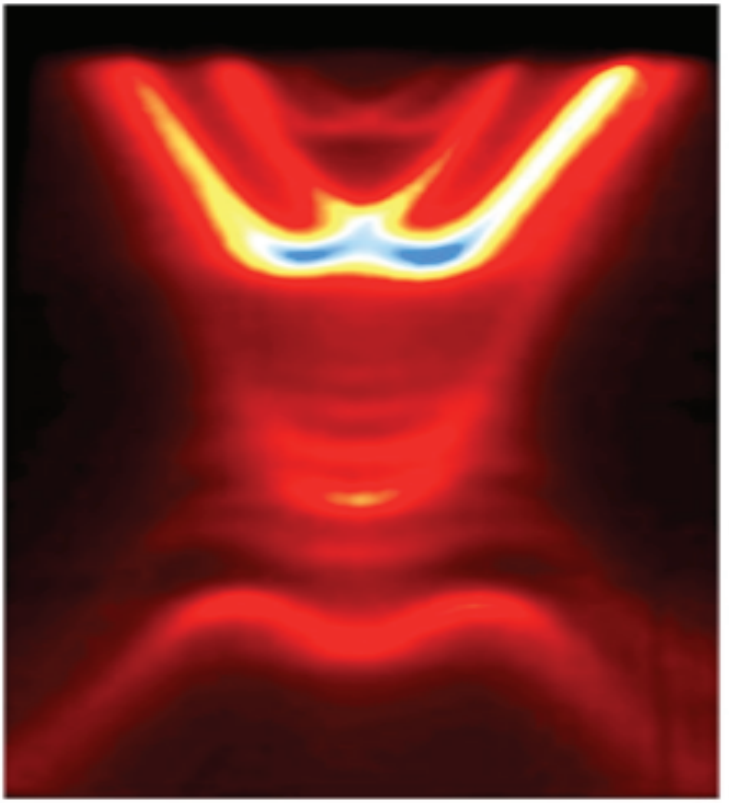

Surface Physics: An Introduction

Written and published by Philip Hofmann

ISBN 978-87-996090-1-7

Contents

Preface

The scope of this book is to give an introduction into the physics of solid, crystalline surfaces as well as an overview over the experimental techniques used to study such surfaces. Theoretical concepts are only briefly introduced when they are needed. The main focus lies on the phenomena and their experimental investigation. The text covers only a fraction of the field and the choice is rather subjective. The most important physical phenomena and experimental techniques should be covered, however.

There are many other general books on surface physics. Here are some that can serve for further reading:

- Modern Techniques of Surface Science by T. A. Delchar, and D. P. Woodruff, Cambridge Solid State Science Series, 1994.
- Physics at Surfaces by A. Zangwill, Cambridge Univ. Press, 1988.
- Solid Surfaces, Interfaces and Thin Films by H. Lüth, Springer, 2010.
- Concepts in Surface Physics by M. C. Desjonqueres, D. Spanjaard, Springer, 2012.
- Physics of Surface and Interfaces by H. Ibach, Springer, 2006.

A more specific list for further reading is given in the end of each Chapter and some references are given in the text. Note, however, that this is a textbook and not a review article and the references are merely intended to help you with finding a more in-depth discussion of the subjects.

Each Chapter ends with a list of discussion questions you can use to test your understanding of the text and with a few problems to further deepen your understanding of the concepts introduced. The problems marked by (*) are more difficult and meant as a challenge.

This book is self-published as an ebook and both of these concepts are new to me. My hope is that this new approach of publishing will provide the student with a useful text at at more affordable price than the usual textbooks, while at the same time ensuring that the costs for the technical realisation, ISBN numbers, distribution and so are covered. An important issue for this approach to publishing is quality control, something that

can only be ensured through testing. I am therefore very grateful to my colleagues Jeppe Vang Lauritsen at Aarhus University and Christoph Tegenkamp at the University of Hannover, as well as their students, for using a previous version of the book in their courses and for providing valuable feedback and corrections.
I gratefully acknowledge the help from my colleagues David Adams and Flemming Besenbacher who I initially joined in teaching the surface science course at Aarhus University. I have used several electronic pictures from David here. Many of the other images have been made by Erik Holst Mortensen. Over the years, many other colleagues have contributed with valuable suggestions, discussions, examples and figures to the development of this text. I specifically acknowledge the input from Alessandro Baraldi, Silvano Lizzit, Justin Wells, Ivan Stensgaard, Erik Lægsgaard, Lars Petersen, Anders Tuxen, Georg Enevoldsen, Jeppe Lauritsen, Liv Hornekær, Søren Ulstrup, Marco Bianchi, Meike Stöhr, Philip King, Karsten Pohl, Wolfgang Theis, Federico Rosei, Carsten Busse and Anton Tamtögl. I also thank the many students who have followed the surface science course and contributed with corrections and suggestions. Finally, I would like to thank my PhD and postdoctoral supervisors Alex Bradshaw, Phil Woodruff and Ward Plummer who introduced me to the subject of surface physics.

Chapter 1

Introduction

This book gives a brief introduction into the physics of solid surfaces their experimental study. Surfaces and interfaces are everywhere and many surface-related phenomena are common in daily life (texture, friction, surface-tension, corrosion, heterogeneous catalysis). Here we are concerned with understanding the microscopic properties of surfaces, asking questions like: what is the atomic structure of the surface compared to that of the bulk? What happens to the electronic properties and vibrational properties upon creating a surface? What happens in detail when we adsorb an atom or a molecule on a surface? In some cases, establishing a connection to the macroscopic surface phenomena is possible. In others, the microscopic origin of these phenomena is not understood in detail. We will mostly concentrate on simple model systems like the clean and defect-free surface of a single-crystal substrate. Such things do of course only exist in our imagination but the technological progress in the last 50 years has made it possible for model experiments to get quite close to this ideal. This together with the progress in surface science theory makes it meaningful to compare experimental results to quantitative calculations.

One of the most important motivations in surface science is the understanding of heterogeneous catalysis. The fact that the presence of a solid could accelerate a chemical reaction without modifying the solid was first discovered in the early 19th century. Knowledge about catalysis has then rapidly grown and been the basis of the developing chemical industry. In the beginning, the microscopic mechanism of the catalytic process was, of course, unknown. Much was tried and "good" catalysts were made from experience. A typical surface science experiment on an "ideal" single crystal surface in ultra-high vacuum is rather far away from the conditions a real catalyst is working in: the

catalyst may be made of small metal particles dispersed on an inert substrate in a high gas pressure and at elevated temperature. Nevertheless, the surface science approach can give important information about many fundamental processes in catalysis. But there are of course situations where this is not enough. Therefore one tries to move into a direction where one is closer to the real catalyst but still very controlled. One can, for example, study the catalytic properties of well-defined metal clusters on a well-defined surface. The ultimate goal is of course to really understand the catalytic reaction in all steps and to improve the catalyst (make it cheaper or more efficient). Closely related to this is the issue of corrosion. Questions are: What are the chemical reactions leading to corrosion? How do they take place on the surface and what can we do to prevent them?

Another reason for the strong interest in surfaces is related to the semiconductor industry. There is a need to build ever smaller structures in order to achieve higher integration on computer chips. One consequence of small structures is that the relative importance of the surfaces is increasing. Another, more practical, consequence is the need to build these structures with high precision and to have flat interfaces between them. This is also an issue in the growth of thin and ultra-thin films and multilayers needed for semiconductors, magnetic storage, coatings and so on. Surface Science research on semiconductor surfaces is much closer to the real technological world than the research in heterogeneous catalysis. Most semiconductor devices are build starting from single-crystal silicon wafer. Related to the increased importance of surfaces in connection to smaller semiconductor structures is the field of nano technology. The electronic properties of nano structures are governed by quantum-confinement effects and the surface sets up the boundary conditions. In some cases, it is even such that surface-localised electronic states dominate the electronic properties of a nano object.

A more fundamental issue is that surfaces and interfaces provide a unique opportunity to study (nearly) two-dimensional electronic systems. The most famous examples for this is quantum Hall effect where a two-dimensional electron gas is generated in a semiconductor heterostructure. Such a two-dimensional electron gas can also be created near a surface and studied with a range of powerful surface science techniques. Another opportunity to study electronic phenomena in (nearly) two dimensions are surface-localised electronic states that exist on many pristine surfaces.

Chapter 2

From Solids to Surfaces

2.1 Introduction

In the present Chapter, we briefly review the basic ideas of solid state physics and establish a link to our actual subject, the physics of solid surfaces. It is assumed that you have already followed a basic course on solid state physics. Hence, any detailed treatment is omitted and we merely focus on some "highlights".

When trying to learn something about solids, the biggest problem one encounters is that a macroscopic solid contains very many (10^{23}) atoms. It is therefore impossible to solve any equations of motion, classical or quantum, in a direct way. The key for a quantitative description of the electronic and vibrational properties of solids is the fact that most solids are crystals and the crystal symmetry can be exploited to greatly facilitate the solution of the problem. This Chapter thus reminds you about the description of crystals in real and reciprocal space and it explains some basic ideas relating the surface properties to those of the bulk.

We divide the properties of a solid into electronic contributions and lattice vibrations. This division is not without problems: In principle one would have to solve the Schrödinger equation for the whole system, with the co-ordinates of all the electrons and all the ions. The reason why separating the electronic and vibrational degrees of freedom works well, is that the ions are so much heavier and slower than the electrons. When the ions move out of their equilibrium-position the electrons follow quickly but they stay in their ground state. They just move to another ground-state with higher energy. When the ions are moving back, the electrons follow to their initial ground state. The good approximation that the electrons remain in their ground state is called *adiabatic* or *Born-Oppenheimer*

approximation.
The mass difference is also reflected in the different energy scales in electron and ion motion: typical kinetic energies of electrons are in the region of several eV while the vibrational (phonon) energies are several meV. The strategy to follow is therefore to solve the electronic structure assuming a rigid crystal. Then the vibrational properties can be calculated from the known electronic properties. Finally, the influence of the vibrational states on the electronic system can be considered: it is usually just a very small (but potentially important!) change.

2.2 Lattice and reciprocal lattice

2.2.1 Lattice

Many solids exist in a crystalline form. Not only the ones that appear as large single crystals in nature (like diamond, many minerals and salts) but also metals grow as crystals, with bigger chunks of material often made from small crystallites with different orientations. Since these crystallites are still much bigger than the atomic spacings, we can view the solids as ideal crystals and use the perfect periodicity to facilitate many of the problems.
We start with some basic definitions. The most fundamental is that of a *Bravais lattice*. It is defined as a lattice of points with position vectors

$$\mathbf{R} = n_1\mathbf{a}_1 + n_2\mathbf{a}_2 + n_3\mathbf{a}_3. \tag{2.1}$$

Examples for a Bravais lattice are the body centred cubic (bcc) lattice and the face centred cubic (fcc) lattice shown in Fig. 2.1.
Given the Bravais lattice, the *primitive unit cell* can be defined: it is any volume of space that, when translated through all the vectors of the Bravais lattice, fills all of space without either overlaps or voids. There are many possible choices for this primitive unit cell. One very common is the *Wigner-Seitz* cell. This cell has the full symmetry of the lattice and is defined as the region of points closer to a given lattice point than to any other lattice point. The Wigner-Seitz cells of the bcc and fcc lattice are also given in Fig. 2.1.
Finally, a real crystal can be described by a Bravais lattice and a so-called *basis*. The basis is a fixed arrangement of atoms or molecules that is placed on every point of the Bravais lattice. It can just be one atom or it can be a whole protein in crystals used for protein structure determination by x-ray diffraction.

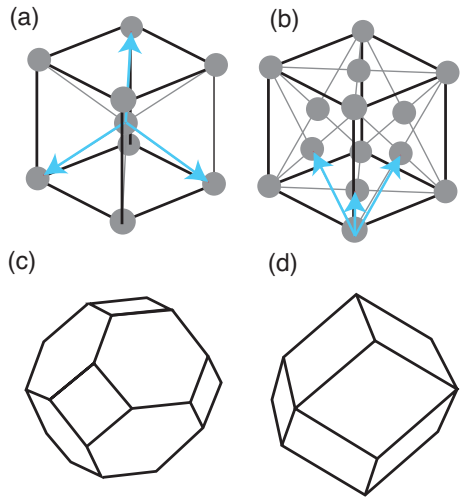

Figure 2.1: (a) The body-centred cubic (bcc) and (b) the face-centred cubic (fcc) Bravais lattice. The vectors spanning the lattices are given as arrows. (c), (d) The Wigner-Seitz cells for the fcc and bcc lattice, respectively.

The basis for the fcc and bcc lattices is just one atom but in order to see this, one has to realise that the cube is not the primitive unit cell. The Bravais lattice vectors actually spanning the primitive unit cells are indicated in Fig. 2.1(a) and (b).

2.2.2 Reciprocal lattice

Starting from the Bravais lattice, the *reciprocal lattice* can be defined as the set of vectors $\mathbf{G}$ that yield plane waves with the periodicity of the Bravais lattice. This means that if $\mathbf{G}$ belongs to the reciprocal lattice of a Bravais lattice with points $\mathbf{R}$ then the relation

$$e^{i\mathbf{G}\cdot(\mathbf{r}+\mathbf{R})} = e^{i\mathbf{G}\cdot\mathbf{r}} \tag{2.2}$$

or

$$e^{i\mathbf{G}\cdot\mathbf{R}} = 1 \tag{2.3}$$

must hold.
The reciprocal lattice vectors also form a Bravais lattice

$$\mathbf{G} \;=\; n_1\mathbf{b}_1 + n_2\mathbf{b}_2 + n_3\mathbf{b}_3. \tag{2.4}$$

and the vectors $\mathbf{b}_1, \mathbf{b}_2, \mathbf{b}_3$ spanning this lattice can be constructed explicitly by

$$\mathbf{b}_1 = 2\pi \frac{\mathbf{a}_2 \times \mathbf{a}_3}{\mathbf{a}_1 \cdot (\mathbf{a}_2 \times \mathbf{a}_3)} \qquad \mathbf{b}_2 = 2\pi \frac{\mathbf{a}_3 \times \mathbf{a}_1}{\mathbf{a}_1 \cdot (\mathbf{a}_2 \times \mathbf{a}_3)} \qquad \mathbf{b}_3 = 2\pi \frac{\mathbf{a}_1 \times \mathbf{a}_2}{\mathbf{a}_1 \cdot (\mathbf{a}_2 \times \mathbf{a}_3)} \tag{2.5}$$

From this, it is easy to derive the very useful relation.

$$\mathbf{a}_i \cdot \mathbf{b}_j = 2\pi \delta_{ij}. \tag{2.6}$$

For the examples in Fig. 2.1, one finds that the reciprocal lattice of the fcc Bravais lattice is the bcc lattice and for the bcc Bravais lattice, it is the fcc lattice.
The concept of the reciprocal lattice allows us to re-write many solid state problems in a much simpler way by making use of the crystal symmetry. Take for example a one-dimensional lattice with lattice spacing a. A periodic function on this lattice, such as the charge density, fulfils

$$\rho(x) = \rho(x + na), \tag{2.7}$$

with n being an integer number. ρ can be written in a Fourier series

$$\rho(x) = \textstyle\sum_n \rho_n e^{i(n2\pi/a)x}, \tag{2.8}$$

where $2\pi/a$ is the distance between the points of the one-dimensional reciprocal lattice. For the analogous three-dimensional charge density

$$\rho(\mathbf{r}) = \rho(\mathbf{r} + \mathbf{R}), \tag{2.9}$$

the same construction can be made with the sum taken over the reciprocal lattice vectors $\mathbf{G}$

$$\rho(\mathbf{r}) = \textstyle\sum_{\mathbf{G}} \rho_{\mathbf{G}} e^{i\mathbf{G}\cdot\mathbf{r}}. \tag{2.10}$$

At first glance, the advantage of writing down this series may not be obvious: In real space we have to describe ρ for every point in the unit cell and there are, in principle, infinitely many points, but in reciprocal space we also have an infinite series. However, it turns out that it is often sufficient to use very few Fourier coefficients to get an accurate description of ρ.
It is also possible to define a primitive unit cell in the reciprocal lattice. Of special importance in the theory of electronic and vibrational states is the Wigner-Seitz cell in the reciprocal lattice. It is called the *first Brillouin zone*. The first Brillouin zones for the bcc and fcc lattice look like the Wigner-Seitz cells for the fcc and bcc lattice in Fig. 2.1, respectively.

Another point worth mentioning in connection with our actual subject, the physics of surfaces, is the definition of the Miller indices. These are used to define a lattice plane or the orientation of a surface plane. A plane can be conveniently defined by a vector perpendicular to the plane and the Miller indices use the reciprocal lattice vectors to do this: the lattice plane with the Miller indices (h, k, l) is the plane perpendicular to the reciprocal lattice vector $h\mathbf{b_1} + k\mathbf{b_2} + l\mathbf{b_3}$. In a simple cubic lattice, the reciprocal lattice is also simple cubic and the $\mathbf{b_i}$ vectors have the same direction as the $\mathbf{a_i}$ vectors. Thus, the (h, k, l) plane is not only perpendicular to the $h\mathbf{b_1} + k\mathbf{b_2} + l\mathbf{b_3}$ vector but also to the $h\mathbf{a_1} + k\mathbf{a_2} + l\mathbf{a_3}$ vector and the construction is trivial (see Fig. 2.2).
For the definition of lattice planes, the bcc and fcc lattice are usually treated as simple cubic but we need to be aware of the possible confusion arising from this. For non-cubic materials it is very important to remember the actual definition of the Miller indices: they give a direction in reciprocal space, not in real space.

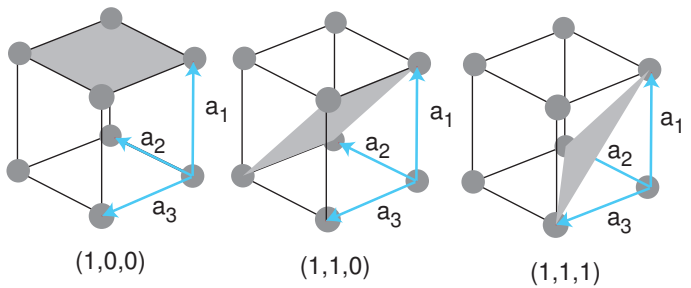

Figure 2.2: Three lattice planes and their Miller indices in the simple cubic lattice.

2.2.3 Directions in real and reciprocal space

There are some conventions for specifying surface orientations and directions on surfaces that are worth summarising here. Surface orientations are generally given by the Miller indices (h, k, l), as illustrated in 2.2 for the simple cubic lattice. Often, the commas in the Miller indices are omitted and one writes (hkl). If the surface direction needs to be specified with a negative index, it can be written as e.g. $(h - kl)$ but often the minus sign is replaced by a bar as in $(h\bar{k}l)$. While the Miller indices in round brackets (hkl) denote a specific direction in reciprocal space and the surface perpendicular to this direction, indices in curly brackets $\{hkl\}$ denote a family of symmetry-equivalent directions or planes. In a cubic crystal, $\{100\}$ could be used in order to refer to the equivalent $(100), (010), (001), (00\bar{1}), (0\bar{1}0)$ and $(\bar{1}00)$ planes.

Similar conventions apply for directions in real space. Square brackets are used to give specific directions. For example $[lmn]$ corresponds to the real space direction $l\mathbf{a}_1+m\mathbf{a}_2+n\mathbf{a}_3$. Again, a bar above a number means minus. Angle brackets are used to denote equivalent directions in real space. As an example, the $[001], [010], [100], [00\bar{1}], [0\bar{1}0]$ and $[\bar{1}00]$ directions could be summarised as the $\langle 001\rangle$ direction.
Finally, it is useful to know that Miller indices for hexagonal structures are often given with four numbers instead of three, i. e. $(hkil)$. In this notations, the last index l refers to the direction of the hexagonal c axis and the additional index i can be calculated by $i = -(h + k)$.

2.2.4 Lattice and reciprocal lattice at surfaces

Now we discuss how to apply the concepts of the Bravais lattice, the basis and the reciprocal lattice to a solid's surface. Cleaving a bulk crystal results in two semi-infinite half-crystals, each terminated by a surface. This affects the global symmetry of the system: parallel to the surface, crystalline translational symmetry is conserved but perpendicular to the surface, it is broken, at least at the actual surface position. The surface as such could be viewed as a perfectly periodic two-dimensional system but very often the three-dimensional character of the bulk under the surface cannot be ignored and the system is effectively between two-dimensional and three-dimensional. We will see several examples of this.
When the surface is formed, one could assume that all the atoms stay at the same positions as before in the bulk. This is actually often not the case but we assume it for now. For the newly formed surface, we now define a two-dimensional Bravais lattice and illustrate this using the example of the fcc(001) surface, i.e. the termination of an fcc crystal with a plane of Miller indices (001). Fig. 2.3 shows how this surface is related to the bulk fcc crystal structure as well as an atomistic model for the surface. It is simple to suggest a two-dimensional Bravais lattice for the surface: It consists for the vectors $\mathbf{a}'_1$ and $\mathbf{a}'_2$. These are perpendicular to each other and have the length $a/\sqrt{2}$, with a being the side length of the bulk cube.
We can also construct the surface Bravais lattice starting from the bulk Bravais lattice. The bulk Bravais lattice is given by

$$\mathbf{a}_1 = \frac{a}{2}\begin{pmatrix}0\\1\\1\end{pmatrix}, \quad \mathbf{a}_2 = \frac{a}{2}\begin{pmatrix}1\\0\\1\end{pmatrix}, \quad \mathbf{a}_3 = \frac{a}{2}\begin{pmatrix}1\\1\\0\end{pmatrix}, \tag{2.11}$$

and we are seeking two non-collinear vectors in the surface plane. These can be con-

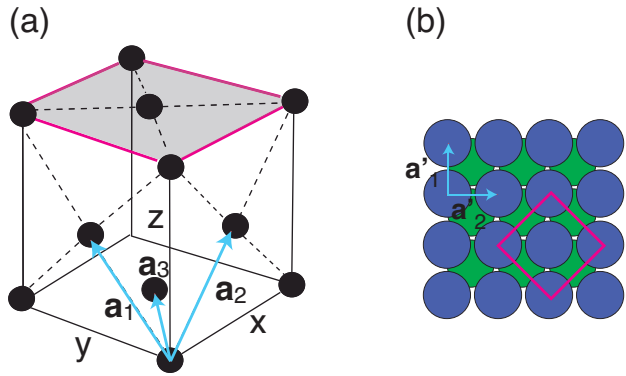

Figure 2.3: The fcc(001) surface. (a) The surface (shaded) in relation to the bulk structure and the vectors spanning the bulk Bravais lattice. Not all the lattice points on the faces of the cube are shown. (b) Top-view of the surface showing the surface Bravais lattice vectors. The purple square corresponds to the top of the cube in (a).

structed by

$$\mathbf{a}'_1 = \mathbf{a}_3 = \frac{a}{2}\begin{pmatrix}1\\1\\0\end{pmatrix}, \quad \mathbf{a}'_2 = \mathbf{a}_1 - \mathbf{a}_2 = \frac{a}{2}\begin{pmatrix}-1\\1\\0\end{pmatrix}, \tag{2.12}$$

i. e. we get the same result as from our naive guess, two vectors that are perpendicular to each other and have the length $a/\sqrt{2}$. It is easily seen that they also have the same directions as the vectors resulting from our direct construction in Fig. 2.3.

What is the basis for the surface? This question is not so easily answered. If we only view the first layer of atoms as "the surface", the definition of the basis is clear enough: Given the Bravais lattice, it would have to contain sufficiently many atoms that we can describe all the atoms in the surface layer. In our case, this would be just one atom, of course. If, however, we are interested in the atoms of deeper layers as well, we could have to include them in the basis. A pragmatic approach to this would be to define the crystal as a stack of identical units, possibly made of several atomic layers, with the same basis for each unit.

The construction of the surface reciprocal lattice is illustrated using the same example of the fcc(001) surface in Fig. 2.4. We can directly construct the vectors spanning the surface reciprocal lattice $\mathbf{b}'_1$ and $\mathbf{b}'_2$ from the surface Bravais lattice vectors $\mathbf{a}'_1$ and $\mathbf{a}'_2$ using (2.6). We immediately see that $\mathbf{b}'_1$ must be perpendicular to $\mathbf{a}'_2$ and hence parallel to $\mathbf{a}'_1$. Moreover, $\mathbf{b}'_1 \cdot \mathbf{a}'_1 = 2\pi$ and therefore the length of $\mathbf{b}'_1$ must be $2\pi\sqrt{2}/a$. $\mathbf{b}'_2$ has the same length and is perpendicular to $\mathbf{b}'_1$.

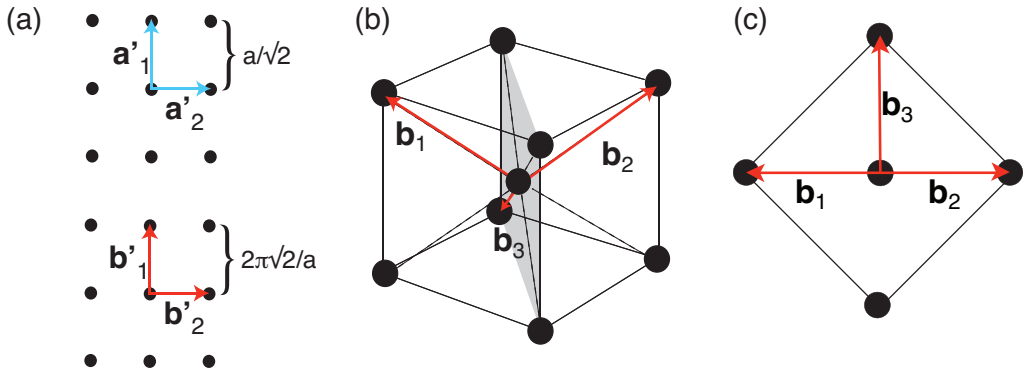

Figure 2.4: (a) Construction of the surface reciprocal lattice for the fcc(001) surface directly from the real space Bravais lattice in the plane of the surface. (b) The fcc reciprocal lattice. The surface plane is the top of the cube and the surface reciprocal lattice can be obtained by projecting the bulk reciprocal lattice vectors onto this plane. The grey plane is the same as in Fig. 2.5. (c) The result of this projection, i.e. the cube in (b) viewed from the top.

We can also obtain the surface reciprocal lattice from a projection of the bulk reciprocal lattice onto the surface plane. The bulk reciprocal lattice of the fcc lattice is a bcc lattice, as illustrated in Fig. 2.4. Explicitly, it is given by

$$\mathbf{b}_1 = \frac{2\pi}{a}\begin{pmatrix} -1 \\ 1 \\ 1 \end{pmatrix}, \quad \mathbf{b}_2 = \frac{2\pi}{a}\begin{pmatrix} 1 \\ -1 \\ 1 \end{pmatrix}, \quad \mathbf{b}_3 = \frac{2\pi}{a}\begin{pmatrix} 1 \\ 1 \\ -1 \end{pmatrix}, \tag{2.13}$$

A normal vector perpendicular to the surface is

$$\mathbf{n} = \begin{pmatrix} 0 \\ 0 \\ 1 \end{pmatrix}. \tag{2.14}$$

Note, that this vector is obviously perpendicular to the surface we are interested in here (it is directed along the z axis) but this direction is not consistent with the (hkl) reciprocal lattice vector being perpendicular to the surface. In fact, only the (110) reciprocal lattice vector would be perpendicular to the surface. The reason is that we have defined our (001) surface with respect to the cubic unit cell, as one usually does for fcc and bcc surfaces, and not with respect to the primitive unit cell. This is a convenient convention but one has to keep in mind that it is applied here!

In order to project the reciprocal lattice out onto the surface, we take each reciprocal lattice vector and subtract the component of this vector that is perpendicular to the surface. For $\mathbf{b}_1$ we get

$$\mathbf{b}_1 - \mathbf{b}_1 \cdot \mathbf{n} = \frac{2\pi}{a} \begin{pmatrix} -1 \\ 1 \\ 1 \end{pmatrix} - \frac{2\pi}{a} \begin{pmatrix} -1 \\ 1 \\ 1 \end{pmatrix} \cdot \begin{pmatrix} 0 \\ 0 \\ 1 \end{pmatrix} = \frac{2\pi}{a} \begin{pmatrix} -1 \\ 1 \\ 0 \end{pmatrix} \tag{2.15}$$

and for the two other vectors we get

$$\mathbf{b}_2 - \mathbf{b}_2 \cdot \mathbf{n} = \frac{2\pi}{a} \begin{pmatrix} 1 \\ -1 \\ 0 \end{pmatrix}, \quad \mathbf{b}_3 - \mathbf{b}_3 \cdot \mathbf{n} = \frac{2\pi}{a} \begin{pmatrix} 1 \\ 1 \\ 0 \end{pmatrix}. \tag{2.16}$$

All of these vectors have the same length as inferred when we directly calculated the surface reciprocal lattice from the surface Bravais lattice. The first two are pointing in opposite directions, perpendicular to the third one. We thus get two independent vectors for the surface reciprocal lattice.

It is curious that we have to project the bulk reciprocal lattice onto the surface in order to get the correct surface reciprocal lattice whereas we merely take one plane (and not the projection) of the real space Bravais lattice in order to obtain the surface Bravais lattice. It is immediately clear why projecting the real space lattice onto the surface plane is not a good idea: this would lead to too many Bravais lattice points since it matters in which layer the points are. For the reciprocal lattice, on the other hand, a projection onto the surface becomes necessary because the periodicity in the direction perpendicular to the surface is lost and hence the quantum number k perpendicular to the surface loses its meaning: It does not matter what value k has in this direction, only the components of the initial $\mathbf{k}$ parallel to the surface retain their meaning.

The necessity for projecting out the reciprocal lattice is illustrated in Fig. 2.5(a). Again, we see how the $\mathbf{b'}_1$ surface reciprocal lattice vector is obtained by the projection of the $\mathbf{b}_3$ bulk reciprocal lattice vector in a cut through reciprocal space. If the value of k perpendicular to the surface is irrelevant, surface reciprocal space points that differ by $\mathbf{b'}_1$ must be completely equivalent. We can see that this is the case when considering the black dots representing the bulk reciprocal lattice points. When projecting the lattice of black dots onto the line parallel with $\mathbf{b'}_1$, this vector does indeed connect two dots.

Having defined the surface reciprocal lattice, we can go on and define the *surface Brillouin zone*. This is the surface analogue to the first Brillouin zone in the bulk and defined in the same way, merely in two dimensions. For a square lattice, the surface Brillouin zone

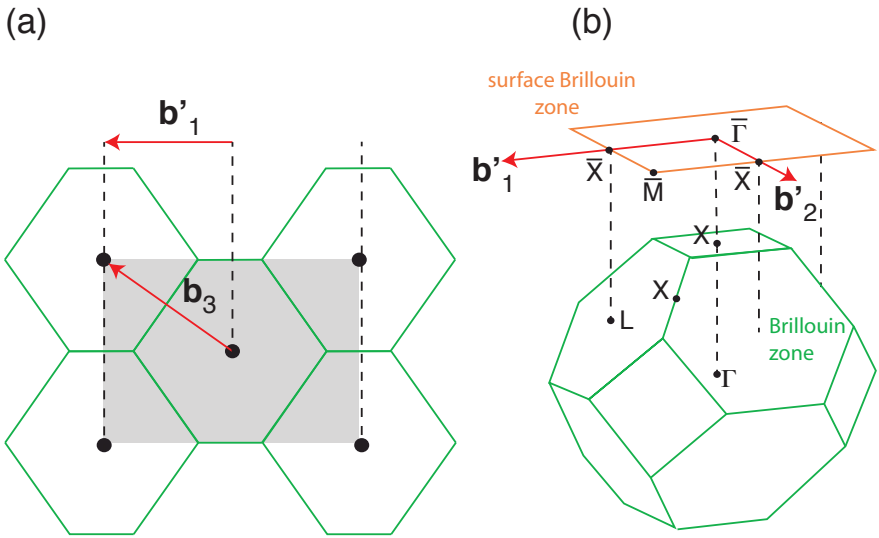

Figure 2.5: (a) Two-dimensional cut through the fcc reciprocal lattice in the grey plane of Fig. 2.4(b), showing the reciprocal lattice points and a cut through the bulk Brillouin zones (in green). The $\mathbf{b}'_1$ surface reciprocal lattice vector is obtained by the projection of the $\mathbf{b}_3$ onto the surface and it connects bulk reciprocal lattice points that are projected out onto the surface. (b) Sketch of the fcc bulk Brillouin zone and the projection on the (001) surface, giving rise to the surface Brillouin zone for fcc(001).

is also a square. Figure 2.5(b) shows the surface Brillouin zone for the fcc(001) surface in relation to the bulk Brillouin zone. Note that the surface Brillouin zone is parallel to the square face of the bulk Brillouin zone, but it is larger than this square. Why this is so is obvious when we consider that the surface reciprocal lattice is a projection of the bulk reciprocal lattice. The edge point of the surface Brillouin zone (the $\bar{X}$ point) must project down to the centre of the hexagon on the bulk Brillouin zone (the L point) because this point is at half the distance between two projected bulk Brillouin zone centre points. This is also evident from the cut in Fig. 2.5(a).

The high symmetry points of the bulk Brillouin zone are typically denoted by letters such as Γ for the centre and X,L and so on for points on the faces. For the surface Brillouin zone, similar notations are used but the two-dimensional high symmetry points carry a bar over the letter. The centre of the zone, for example, is called Γ in the bulk and $\bar{\Gamma}$ on the surface.

For all the above considerations, we have assumed that the atoms near the surface simply

remain at the position they had in the bulk solid when the surface is formed. This does not have to be so: Imagine the forces on an atom at the new surface. The atom loses some of its nearest neighbours and an entirely new energetic situation arises. The first layer atoms could move further away from the remaining neighbours or closer towards them. Such a change of the first interlayer spacing is a called a *relaxation*.
Not even the periodicity parallel to the surface needs to remain the same as in the bulk: On many surfaces, especially on semiconductors, the atoms try to find new "partners" for the broken bonds sticking into the vacuum. This can lead to a *reconstruction* of the surface where the periodicity parallel to the surface is not the same as in the bulk. We will discuss this in more detail in Section 7.2.
We conclude this section by again illustrating the usefulness of the reciprocal lattice, now with special emphasis to the two-dimensional surface reciprocal lattice. Figure 2.6(a) shows a Scanning Tunnelling Microscopy (STM) image of a Pt(111) surface and Fig. 2.6(b) shows the Fourier transformation of this image. Pt is an fcc metal and the (111) surface is a closed-packed surface with hexagonal symmetry. At this point, we do not have to worry how an STM works or what exactly the picture shows. We can merely interpret it at the charge density at the surface, resolved on an atomic scale. The charge density varies with the periodicity of the atomic lattice, it is highest where the atoms are and we can interpret Figure 2.6(a) as "an image of the atoms". A Fourier transform of the charge density should basically be an image of (2.10) with the intensity at the reciprocal lattice spots being equal to the (magnitude of the) Fourier coefficients of the charge density. This is indeed the case. We can see that the six spots around the origin are by far the most intense features. They alone give already a decent description of the entire STM image. This makes the usefulness of reciprocal space obvious. When looking closer, weaker features at other reciprocal lattice points can be seen.

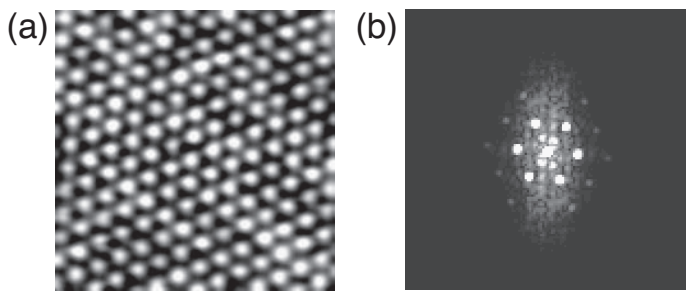

Figure 2.6: (a) Scanning tunnelling microscopy image of Pt(111). (b) The Fourier transformation of this image [1].

2.3 Electronic states

We briefly recapture different approaches to describe the electronic structure of solids. In all of these it is assumed that the situation can be described by one electron moving in the potential of the ions and all the other electrons. For metals, the electrons are largely free and the electronic states can often be well-described by assuming either completely free electrons (i.e. a vanishing crystal potential) or nearly free electrons. For more covalently bonded materials, on the other hand, the electrons are still strongly bound to their respective atoms and a simple description starts from a linear combination of the atomic orbitals. Ultimately, all approaches lead to a dispersion of the electronic levels in reciprocal space, i. e. to a number of energy bands $E_n(\mathbf{k})$, where the index n numbers the bands.
Once we have obtained these bands, they are filled up with the available electrons according to the Fermi-Dirac distribution

$$f(E,T) = \left(e^{\frac{E-\mu}{k_B T}} + 1\right)^{-1}, \tag{2.17}$$

where μ is the (temperature-dependent) chemical potential that, for a metal, is approximately equal to the (temperature-independent) Fermi energy E_F, the highest energy reached when filling in the electrons at $T = 0$.

2.3.1 Free electrons

A possible starting point for a quantum mechanical treatment of the solid's electronic structure is to consider free electrons in a box. It can be assumed that this is an appropriate model to describe a metal. We calculate single particle states and neglect the electron-electron interaction. We can assume a vanishing potential in the box and the Schrödinger equation is

$$H\psi(\mathbf{r}) = -\frac{\hbar^2}{2m_e}\nabla^2\psi(\mathbf{r}) = E\psi(\mathbf{r}). \tag{2.18}$$

The solution must have the form

$$\psi(\mathbf{r}) = Ae^{i\mathbf{k}\cdot\mathbf{r}} + Be^{-i\mathbf{k}\cdot\mathbf{r}}, \tag{2.19}$$

where A and B are complex amplitudes. This gives rise to the energy eigenvalues

$$E(\mathbf{k}) = \frac{\hbar^2|\mathbf{k}|^2}{2m_e} = \frac{\hbar^2}{2m_e}(k_x^2 + k_y^2 + k_z^2) \tag{2.20}$$

The possible values of $\mathbf{k}$ are restricted by the choice of boundary conditions. We can, for example, require that the wave function must vanish at the border of the box, as would be the case for an infinitely high potential barrier. Then A and B in (2.19) are chosen such that the wave functions are of the form

$$\psi(\mathbf{r}) \propto \sin k_x x \sin k_y y \sin k_z z, \tag{2.21}$$

and the $\mathbf{k}$ values are

$$\begin{aligned} k_x &= \tfrac{\pi}{L} n_x;\ n_x = 1, 2, 3, \dots \\ k_y &= \tfrac{\pi}{L} n_y;\ n_y = 1, 2, 3, \dots \\ k_z &= \tfrac{\pi}{L} n_z;\ n_z = 1, 2, 3, \dots, \end{aligned} \tag{2.22}$$

where L is the side length of the box, that is assumed to be a cube.
Alternatively, we can use periodic boundary conditions, i.e.

$$\psi(\mathbf{r}) = \psi(x, y, z) = \psi(x + L, y, z) = \psi(x, y + L, z) = \psi(x, y, z + L), \tag{2.23}$$

with the solutions of (2.18) written as

$$\psi(\mathbf{r}) \propto e^{i\mathbf{r}\cdot\mathbf{k}} \tag{2.24}$$

and the permitted $\mathbf{k}$-points are

$$\begin{aligned} k_x &= \tfrac{2\pi}{L} n_x;\ n_x = 0, \pm 1, \pm 2, \pm 3, \dots \\ k_y &= \tfrac{2\pi}{L} n_y;\ n_y = 0, \pm 1, \pm 2, \pm 3, \dots \\ k_z &= \tfrac{2\pi}{L} n_z;\ n_z = 0, \pm 1, \pm 2, \pm 3, \dots . \end{aligned} \tag{2.25}$$

This choice of boundary conditions has no effect on the resulting properties. If we, for example, calculate the density of states, we get exactly the same result. From a surface point of view, this appears to be a problem because it should make a difference if we force the wave functions to vanish at the surface or not. We discuss this in some more detail below, but here we just point out that these boundary conditions are not intended to represent a solid with a surface. Indeed, their purpose is to give an accurate description of a bulk solid, avoiding the difficulty of having a surface.

2.3.2 Electrons in a periodic potential: Nearly free electrons

In a real crystal, the potential is not zero or constant. We do not usually know its precise form but we do know that it has the same periodicity as the lattice. The Schrödinger equation is

$$H\psi(\mathbf{r}) = (-\tfrac{\hbar^2}{2m_e}\nabla^2 + U(\mathbf{r}))\psi(\mathbf{r}) = E\psi(\mathbf{r}) \tag{2.26}$$

where $U(\mathbf{r}) = U(\mathbf{r}+\mathbf{R})$ is the potential. The solutions of this equation are *Bloch waves* with the form

$$\psi_{\mathbf{k}}(\mathbf{r}) = u_{\mathbf{k}}(\mathbf{r})e^{i\mathbf{k}\cdot\mathbf{r}} \tag{2.27}$$

where $u_{\mathbf{k}}(\mathbf{r}) = u_{\mathbf{k}}(\mathbf{r}+\mathbf{R})$ is a lattice periodic function. A general property of the Bloch waves is that

$$\psi_{\mathbf{k}}(\mathbf{r}) = \psi_{\mathbf{k}+\mathbf{G}}(\mathbf{r}) \tag{2.28}$$

where $\mathbf{G}$ is a reciprocal lattice vector. This means that a Bloch wave does not change when it is shifted by a reciprocal lattice vector. Inserting this into the Schrödinger equation gives that also

$$E_{\mathbf{k}} = E_{\mathbf{k}+\mathbf{G}}. \tag{2.29}$$

Since both the wave-functions and the energies are periodic in reciprocal space it is sufficient to treat both in the first Brillouin zone.
For a simple approach to the electronic structure of metals, one can assume that the potential is very weak, i.e. that the electrons are nearly free. The green dashed lines in Fig. 2.7(a) are the resulting bands for such a potential in a one-dimensional lattice of periodicity a. The bands are merely parabolas, i.e. the solutions for the free electron case (2.20). However, there is not only one parabola centred at $k = 0$, but repeated parabolas with a distance of $2\pi/a$ in order to fulfil the requirement (2.29).
This electronic structure changes in an important way if the potential in (2.26) is not almost zero but takes on a finite value. The lattice periodic potential is described by the Fourier series

$$U(\mathbf{r}) = \textstyle\sum_{\mathbf{G}} U_{\mathbf{G}} e^{i\mathbf{G}\cdot\mathbf{r}}. \tag{2.30}$$

If we take a one-dimensional real potential and assume that just the first Fourier coefficient is non-zero, i.e. $U_1^* = U_{-1}$, we find that free electron band picture in Fig. 2.7(a) changes, but only in the immediate vicinity of the Brillouin zone boundaries where *gaps* appear in the band structure. The size of the splitting is twice the magnitude of the Fourier coefficient U_1 in the potential. If we include more non-zero Fourier coefficients, we get gap openings at other degeneracy points. A finite U_2, for example, removes the degeneracy of the next band crossing at $k = 0$. The solid black band structure in Fig. 2.7(a) shows this situation where both $U_1^* = U_{-1}$ and $U_2^* = U_{-2}$ are different from zero.
The opening of band gaps is of fundamental importance for describing the electronic structure of solids because it gives the possibility to describe not only metals but also

semiconductors and insulators. For surfaces, band gaps are also very important because their presence is a necessary condition for the existence of new, surface-localised electronic states as we shall see in Chapter 8.

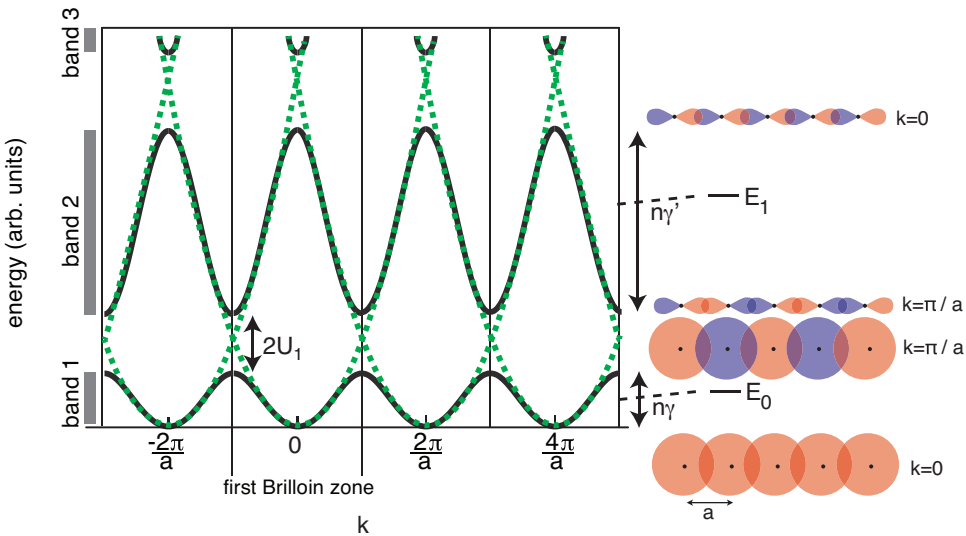

Figure 2.7: Electronic band structure for a one-dimensional periodic potential of lattice constant a. The dashed green lines are the solution for a periodic but vanishingly small potential. The black lines are the solution for nearly free electrons with non-vanishing Fourier coefficients U_g and gaps opening around crossings of the dashed bands. The right hand side illustrates how a similar band structure is arrived at in a tight-binding model, starting from the atomic energy levels E_0 and E_1. These levels are shifted slightly and broadened into bands of the width $n\gamma$ and $n\gamma'$, respectively, where n is the number of nearest neighbours and γ, γ' are determined from the overlap between the wave functions and atomic potentials at neighbouring sites. The Bloch wave functions are derived from the atomic orbitals and they are illustrated for the two lowest lying band (s and p) on the right hand side.

2.3.3 Electrons in a periodic potential: tightly bound electrons

So far, we have viewed the development of band structure by starting from free electrons and then introducing a (weak) lattice potential that gives rise to deviations from the free

Chapter 3

Ultra High Vacuum (UHV)

The key-ingredient to surface science experiments is ultra-high vacuum. This means a pressure in the 10^{-9} mbar range and below. Only such a low pressure will ensure that a surface stays clean for a time long enough to do typical surface science experiments. In the following, the requirement for UHV and some important parts of UHV technology are described. We also discuss how to obtain a clean surface in the first place.

3.1 Vacuum requirements

We can quickly estimate the vacuum requirements for surface science. Let us imagine a clean surface in the vacuum vessel. From kinetic gas theory, we can obtain the number of gas molecules impinging on the surface as

$$R = \frac{dN}{dt} = \frac{P}{\sqrt{2\pi M k_B T}}, \tag{3.1}$$

where M is the molecular mass. The usual units for the pressure in vacuum technology are torr or mbar (1 torr = 1.3332 mbar = 133.32 Pascal). For a pressure of 10^{-6} mbar and a temperature of 300 K, we find the rates of impinging molecules that are given in Table 3.1.
As an order of magnitude value, a surface has 10^{15} atoms per square centimetre. This means that if every rest-gas molecule from the incoming flux sticks to the surface, the latter will only stay clean for a second or so. If we are not willing to tolerate more than, say, one percent of contaminating rest-gas molecules on the surface an hour after cleaning it, then the pressure has to be in the UHV region.

molecule	M_u	R($cm^{-2}s^{-1}$)
H_2	2	$1.1x10^{15}$
H_2O	18	$3.6x10^{14}$
CO	28	$2.9x10^{14}$
O_2	32	$2.7x10^{14}$
CO_2	44	$2.3x10^{14}$

Table 3.1: Rate of molecules impinging on a surface in vacuum at a pressure of 10^{-6} mbar.

It is also interesting to calculate the mean free path λ of the molecules in the gas at a given pressure, i.e. the mean distance before hitting another molecule. Again, we use kinetic gas theory and find

$$\lambda = \frac{k_B T}{\sqrt{2}\pi\xi^2 P}, \tag{3.2}$$

where ξ is the molecular diameter.
Depending on the ratio of λ and the typical dimensions of the vacuum system d (10 cm), different flow regimes can be defined when gas passes through the system, e.g. when it is evacuated by a pump. When $\lambda \ll d$, the flow is called viscous. This is always the case at ambient pressure. In the opposite limit, when $\lambda \gg d$, the flow is called molecular. This is the case for typical UHV pressures, where λ is many meters. It means that it is much more likely that a molecule hits the walls of the vacuum vessel than another molecule and this has important consequences for pump technology.

3.2 Construction, pumping and bakeout

Before discussing the technical details of an actual vacuum system, we start with some general considerations and definitions. The objective of vacuum technology is to remove gas from the recipient. A flow of gas can be defined in terms of the volumetric flow dV/dt or, more usefully, the flow rate Q as

$$Q = \frac{d(PV)}{dt}. \tag{3.3}$$

Flow rates are measured in Pa m^3s^{-1} or similar units (one often finds torr for pressure and litres for volume). Using the ideal gas equation, we obtain

$$Q = \frac{d(PV)}{dt} = k_B T \frac{dN}{dt}, \tag{3.4}$$

so this does indeed corresponds to a flow of particles. The flow rate can be used to describe different situations, such as the flow through a tube connecting vacuum system and pump, the removal of particles from vacuum system or an incoming flow of particles due to a leak in the sealing of the system.
The process of evacuating the system can be described as

$$-\frac{dP}{dt} = P\frac{S}{V_C} - Q_0, \tag{3.5}$$

where V_C is the volume of the vacuum chamber, Q_0 some incoming flow of particles discussed below and S the pumping speed. S is measured in m^3s^{-1} but for commercially available pumps it is most frequently quoted in litres per second (ls^{-1}). To see how the pump-down of the system proceeds, we first consider the limit of this equation when Q_0 is so small that we can neglect it. In this case, (3.5) is solved by

$$P(t) = P_0 \exp(-\frac{S}{V_C}t), \tag{3.6}$$

where P_0 is the starting pressure. Such exponential behaviour is indeed found in the beginning of the pumping process but unfortunately it does not continue, even in the case of $Q_0 = 0$. The reason is that the pumping speed of a vacuum pump depends on the pressure. In fact, apart from the pumping speed, vacuum pumps are also characterised by the lowest achievable pressure (the pressure where S approaches zero) and in order to achieve UHV, it is usually necessary to use a combination of pumps with different characteristics, frequently operated in series.
Fig. 3.1(a) shows the pumping diagram for a typical system. A roughing pump is used to pump the system down into the 10^{-3} mbar region. A typical roughing pump is an oil-sealed rotary vane pump. The working principle of this type of pump is illustrated in Fig. 3.2. It is immediately evident that a rotary vane pump will work well in the viscous flow regime but not in the molecular flow regime where the mean free path of the molecules is very long and the chance of the rest gas molecules hitting the small inlet valve of the pump is small. This explains why the lowest reachable pressure with this pump is only 10^{-3} mbar.
The roughing pump is thus used as a first pumping stage in order to establish a pre-vacuum for another type of pump that can operate in the molecular flow regime. The pump of choice for this second stage is a so-called turbomolecular pump (see Fig. 3.3). The pump has a large inlet to its main rotor, increasing the likelihood of molecules entering the pump. The rotor is designed such that the gas molecules collide with the

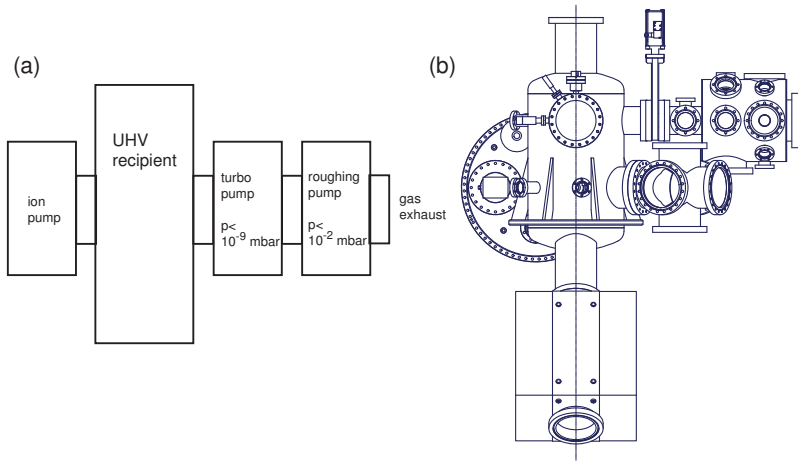

Figure 3.1: (a) Schematic pumping of a typical UHV system. (b) A typical UHV chamber.

fast moving blades and thereby attain some momentum in the direction of the roughing pump. In order to achieve efficient pumping, the rotation speed has to be very high. Typical values are up to 80,000 rotations per minute. The lowest pressure that can be reached with such a pump is in the mid 10^{-11} mbar region. Note, however, that this is only possible if the pre-vacuum pressure from the roughing pump is sufficiently low, because the pressure in the main recipient is influenced by molecules back-flowing through the turbo pump.

Once a low pressure has been achieved, it can also be maintained by another type of pump, the so-called ion pump shown in Fig. 3.4. The rest gas in this pump is ionized by a plasma discharge due to the high voltage between anode and cathode. The ionization probability is increased by the presence of a magnetic field that makes the charged particles travel on spiral trajectories. When the ions hit the titanium cathode, they can be buried in it or react with it. Additionally, titanium is sputtered off the cathode and deposited onto other parts of the pump. This titanium can react with the rest gas and increases the pumping effect. The ion pump does not remove the rest gas from the system. It just binds it such that it cannot contribute to the pressure any more. The current provided by the high-voltage power supply is proportional to the pressure in the system. Ion pumps can therefore also be used to estimate the pressure. The ion pump can be operated at pressures between 10^{-3} and 10^{-11}mbar. Operating the pump at too high a pressure obviously reduces its lifetime.

Another way of "pumping" is the use of a cold trap. This could be any surface in

4.2 Why electrons: The inelastic mean free path

As mentioned above, one of the main motivations to use electrons in surface science is that they allow for surface-sensitive spectroscopy, and the reason for this is their short inelastic mean free path in matter. This inelastic mean free path λ is determined by collisions and defined as in the Drude model for conduction in metals:

$$\lambda(E_{\text{kin}}) = v(E_{\text{kin}})\tau, \tag{4.1}$$

where v is the velocity and τ is the collision time. In the Drude model, τ is the mean time between two scattering events with the ions of the lattice. In a more realistic picture of solids, the (perfect) lattice does not give rise to inelastic scattering but deviations from this perfect lattice do. Then τ is given by the probability of inelastic scattering, no matter by what mechanism.

We are interested in electron energies between a few eV and many hundred eV. The mean free path of the electrons in this regime is plotted in Fig. 4.2. The dashed curve shows a calculation of the mean free path independent of the material and the points are measured data from many elemental solids. The data points scatter around the calculation. The curve is therefore often called a *universal curve*. We shall see that the reason for this universality is that the inelastic scattering of electrons in this energy range is mostly involving excitations of conduction electrons. The inelastic mean free path is related to the conduction electron density and this is quite similar for the elemental solids.

The mean free path curve has a broad minimum around a kinetic energy of about 70 eV (note the log-log scale). There it is less than 10 Å. This means that if we observe an electron with this kinetic energy and this electron has left the solid without suffering an inelastic scattering event, it must originate from the first few atomic layers. Moreover, if we can choose the kinetic energy of the electrons, we can change the surface sensitivity. In the EELS experiment, this can be done because we can vary the kinetic energy of the incoming beam E_0, just by changing the acceleration voltage of the electron gun. If we choose $E_0 \approx 70$ eV, we know that the elastically scattered electrons must have been scattered in the first few atomic layers and we also know that the discrete loss peaks, for example to one particular phonon, must have happened in the first few layers. We can decrease the surface sensitivity either by going to very low energies of only a few eV or to *much* higher energies of a several keV.

In some cases, we do not have the option to change the electron kinetic energy in order to tune the surface sensitivity of the experiment. In this situation, a frequently used

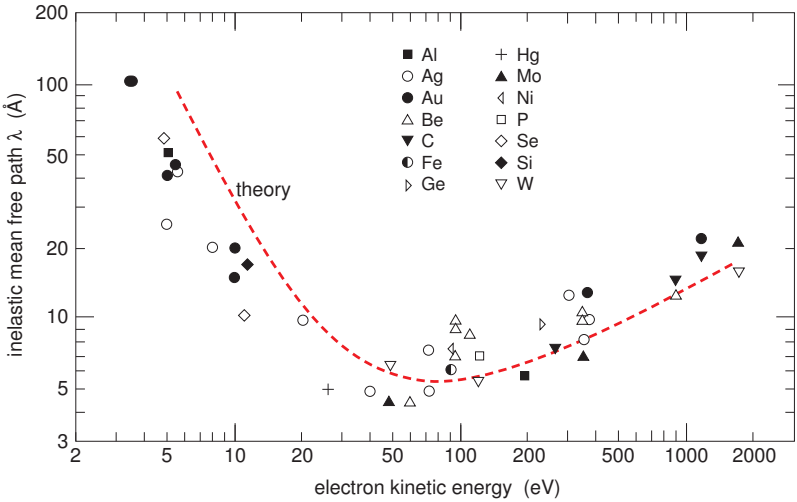

Figure 4.2: The inelastic mean free part of the electrons in solid. The dots are measurements the dashed curve is a calculation. After Ref. [5].

trick is to change the experimental geometry. This is illustrated in Fig. 4.3. With a given inelastic mean free path, we can greatly enhance the surface sensitivity by going to a grazing incidence (or emission) geometry. In this way, the electrons travel mostly close to the surface, even if their mean free path is relatively long.

4.3 Physics of the inelastic mean free path

Let us now consider the interaction of electrons with solids in some more detail in order to understand the basic physics of the electron inelastic mean free path. Before we do this, we briefly discuss the difference between inelastic and elastic scattering and the conditions for the latter process.

In an elastic scattering event the electron's kinetic energy is (by definition) conserved, i.e.

$$E_s = E_0, \tag{4.2}$$

where E_0 is the energy of the incoming electrons and E_s that of the scattered electrons. If we treat the electrons as a particle wave of a certain de Broglie wavelength $\lambda_e = 2\pi/k$, we can apply the usual von Laue scattering theory. In order to observe constructive interference from the scattered electrons, we know that the Laue conditions needs to be

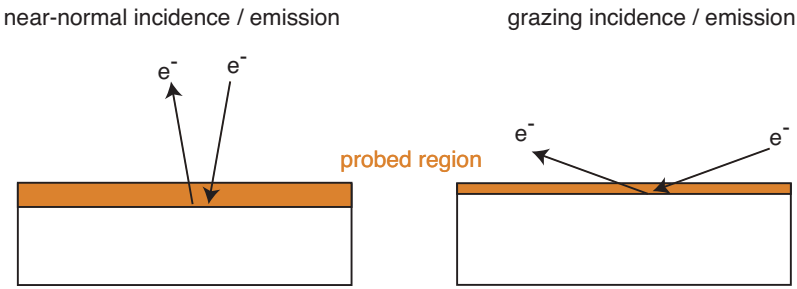

Figure 4.3: With a given inelastic mean free path, the surface sensitivity of a scattering experiment can be influenced by the experimental geometry. The near normal incidence geometry in (a) is considerably less surface sensitive than the gazing incidence geometry in (b).

fulfilled, i.e. $\mathbf{k}' - \mathbf{k} = \mathbf{G}$, where $\mathbf{G}$ is a reciprocal lattice vector and $\mathbf{k}$ ($\mathbf{k}'$) is the wave vector of the incoming (outgoing) electron wave.
However, the Laue conditions are usually derived for infinitely periodic, three-dimensional bulk solids but here we have a situation in which the surface terminates the bulk. As we will discuss in more detail in Chapter 7, this causes the Laue condition perpendicular to the surface to be relaxed, as the periodicity in this direction is lost. We retain a two-dimensional version of the Laue condition, stating that the momentum parallel to the surface is conserved, apart from a surface reciprocal lattice vector $\mathbf{g}$

$$\mathbf{k}_{\|s} = \mathbf{k}_{\|0} + \mathbf{g} \tag{4.3}$$

The crystal itself provides perpendicular momentum such that (4.2) and (4.3) can be fulfilled simultaneously. Observing the elastically scattered electrons provides information about the surface reciprocal lattice and the surface geometry. This is exploited in a technique called low-energy electron diffraction that is explained in more detail in Chapter 7. For the example of the EELS experiment here, we only need to know that the intensity of the elastically scattered beam can be increased strongly if the condition (4.3) is fulfilled.
For now we are more interested in inelastic scattering since it determines the inelastic mean free path of the electrons and hence the surface sensitivity. We can already guess some properties of the dominant scattering events from the shape of the universal curve in Fig. 4.2. The mechanism apparently leads to something "universal" and so it cannot be related to a very specific property of any material. Moreover, the inelastic scattering only severely reduces the mean free path for energies higher than 5 or 10 eV, so this

latter is roughly constant in the region of the atom, the integral will give some finite value. For very high photon energies, on the other hand, the final state wavelength is very short and oscillates (and changes sign) rapidly in the region of the initial state. The product in the overlap integral also oscillates very rapidly with nearly equal positive and negative contributions that average out to zero when the integration is performed.
The only core level that shows a more complex behaviour is the $3p$ level of aluminium. Here the photoemission cross section first decreases but reaches a local minimum, increases again and eventually falls off rapidly. This minimum in the photoemission cross section close to the threshold is called a Cooper minimum. It is only observed for initial states where the radial wave function has a node, e.g. $3p$ but not $2p$.

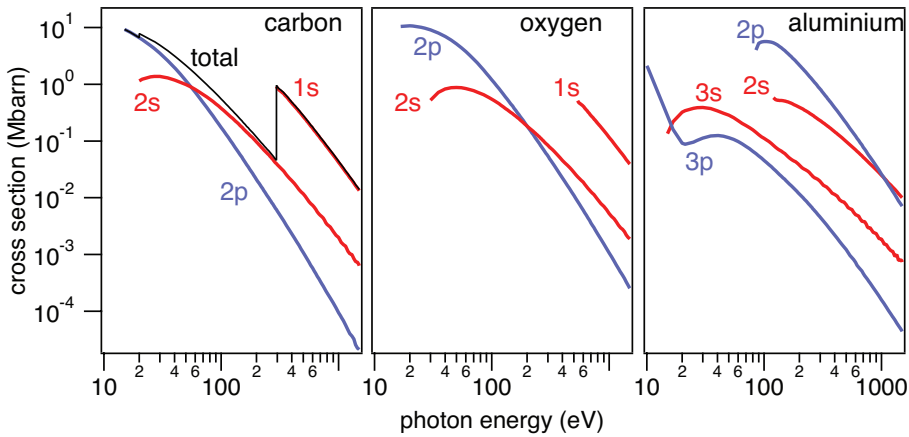

Figure 5.8: Calculated photoemission cross sections as a function of photon energy for carbon, oxygen and aluminium, after Ref. [8].

5.1.3 XPS binding energies

The most important information in XPS is contained in the observed binding energies of the peaks. Not only do they reveal which chemical elements are present, they also give much more subtle information about the chemical environment these elements are in. However, an exact understanding of the observed binding energies is rather complicated. We distinguish between initial state effects and final state effects. The former affect the binding energy of the initial state before the photoemission event, for example by the chemical environment of the atom of interest. The latter are due to the photoemission

event itself and the nature of the final state, i.e. an atom with a missing core electron or something more complex than that.
Before we discuss the detailed origin the binding energy shifts, we briefly address the question why some core level peaks are split into two components and others are not. Such a splitting is caused by the spin-orbit interaction. The spin-orbit interaction is a relativistic effect and thus most important for heavy atoms. The coupling between orbital and spin angular momenta is usually described in either the $L-S$ (or Russel-Saunders) coupling scheme or in the $j-j$ coupling scheme. The $L-S$ coupling is appropriate for light elements, where one couples the orbital and spin angular momenta first to each other, to give the total orbital momentum L and the total spin momentum S and then one combines these to the total angular momentum J. The $j-j$ scheme is applicable if the coupling between orbital and spin angular momenta is so strong that l and s are no longer individual good quantum numbers for each electron but only the total moment j is. Since $s=1/2$, j can be either $l+1/2$ or $l-1/2$. For the resulting j, there are the usual $2j+1$ orientation possibilities. In a p core level, for example, one combines $l=1$ and $s=1/2$ to $j=3/2$ and $j=1/2$ with 4 and 2 possibilities, respectively. This reproduces the 6 expected possible quantum states for p electrons. In an s core level, the orbital angular momentum is zero and hence there is no splitting. In XPS, the coupling scheme of choice is the $j-j$ coupling because the the splitting must be strong in order to be observable and this is only the case for heavy elements where the $j-j$ scheme is more appropriate.
An example of the spin-orbit splitting is given in Fig. 5.9 which shows the $5d$ level of Bismuth. In this case, the splitting is quite substantial, more than 1 eV. The two components correspond to $j=3/2$ and $j=5/2$. The integrated intensity approximately reflects the number of electron states in each component which is 4 and 6, respectively. The anti-parallel alignment of spin and angular momentum ($j=l-s$) is always the more favourable one, hence it has the higher binding energy.
Spin-orbit splitting is an initial state effect and almost entirely atomic in nature. The size of the splitting and the relative intensity of the two components is approximately the same in all compounds of the same element. Hence, it is also useful to identify the core levels in the first place. The close vicinity of two peaks and their intensity ratio can be a hint towards a spin-orbit split core level. The peaks thus cannot stem from an s level and in order to identify the element in question, one can not only use the absolute binding energy of the peak but also the size of the splitting as a characteristic quantity.

For our further discussion of XPS binding energies, we continue with other initial state

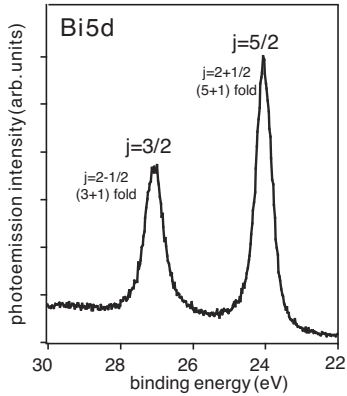

Figure 5.9: Illustration of spin-orbit splitting in XPS using the Bi $5d$ core level.

effects. If one finds, for example, a C $1s$ peak in the XPS spectrum from a surface, then one may be able to decide if the carbon is present in a CO_2 or in a CF_4 molecule. The reason is, that the electronic environment of the carbon atom determines the electrostatic potential at the location of the carbon core level wave function. In the case of CF_4, the F atoms draw the carbon valence electrons strongly away from the carbon. For the $1s$ electron, this leads to an effective increase of the nuclear charge and it therefore increases the binding energy observed in XPS. Fig. 5.10 shows the measured and calculated (see below) binding energies for the C $1s$ peak in different chemical environments. The *chemical shift* over the whole range is rather large, so large that it can even be observed with a conventional x-ray source. Indeed, a shift in a peak can be quite easily observed in any spectroscopic technique, even if the resolution is much poorer than the absolute width of the peak. High resolution is primarily needed to resolve peaks with a small separation.

The use of synchrotron radiation and the thereby achievable high resolution permits the observation of much smaller shifts and additional peaks that are caused by atoms of the same element being in slightly different environments. Fig. 5.11 shows the Ru $3d$ core level spectrum from a *clean* Ru$(10\bar{1}0)$ surface. More precisely, it shows the $j = 5/2$ component that is spectroscopically termed $3d_{5/2}$. Apart from the peak characteristic for ruthenium atoms in their bulk crystal environment, two other peaks are resolved. These can be assigned to emission from the first two atomic layers of this surface. Such *surface core level shifts* (SCLS) are often observed for the transition metals. SCLS both to higher and to lower binding energies are found, so it is not *a priori* obvious which component in the spectrum is caused by the bulk atoms. The fact that the SCLS is

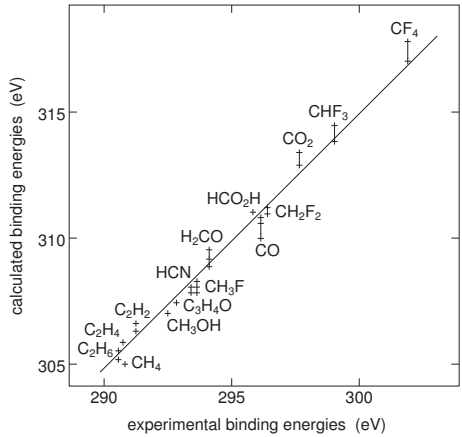

Figure 5.10: Comparison between experimental and calculated (from Koopman's theorem) C $1s$ binding energies. Note that the agreement is very good but only if one of the axes is shifted by 15 eV. The agreement is underlined by the line of slope one. After Ref. [9].

observable at all is immensely useful for surface XPS investigations because it permits a direct spectroscopic access to what is happening to the surface atoms, for example during a chemical reaction.

The sign of the SCLS observed on transition metal surfaces can be explained using the picture given in Fig. 5.12. Transition metals are characterised by a partially filled d-band. When the surface is created, the d-band is narrowed due to the smaller number of nearest neighbours, as expected from the tight-binding picture discussed in Section 2.3. Consider the case of a transition metal at the beginning of the series with a d band that is less than half filled. A band narrowing would move the entire band above the Fermi level. This would mean that the surface is charged: it is at a chemical potential different from the bulk. In order to avoid this energy-expensive situation, there is a flow of charge between the bulk and the surface atoms which leads to an electrostatic potential that shifts the whole d-band down to lower energies. This electrostatic potential does also shift the core levels. The corresponding argument is made for the case of more than half filling. This model largely explains the observed trend over the transition metal series.

So far, we have only considered how the initial state affects the observed binding energy. We have not considered the importance of final state effects or discussed how to calculate the binding energy that we expect to measure in the first place. The most simple assumption for such a calculation is that the measured binding energy is the orbital

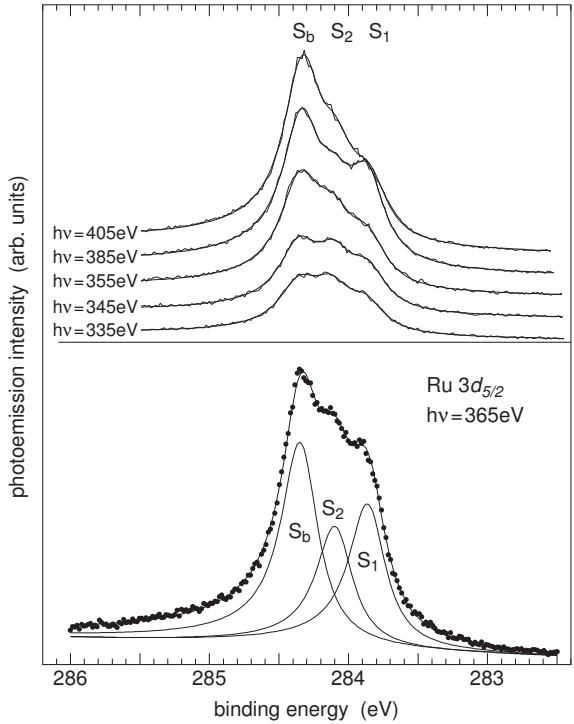

Figure 5.11: A Ru $3d_{5/2}$ core level spectrum from a clean Ru$(10\bar{1}0)$ surface. Apart from the bulk peak S_b, two surface-related peaks are visible, one from the first (S_1) and one from the second layer (S_2). After Ref. [10].

energy of the photo ionised electron. This is known as Koopman's theorem. It is illustrated in Fig. 5.13(a) and it has been used to calculate the binding energies in Fig. 5.10. That Figure shows that the approximation of Koopman's theorem is rather good. When the calculated core level shifts are plotted as a function of the experimental values, all points lie on a line of slope one, implying that the trend of a chemical shift is reproduced correctly. There is, however, a constant offset between the energies. Apparently, the calculated core level binding energies are systematically too high by about 15 eV.

The problem in Koopman's theorem is the following: When an electron is removed from the core state, the other electrons in the system can reach a new ground state. This new ground state has a lower energy due to the increased effective nuclear charge of the photoemitting atom. The *relaxation energy* E_r associated with reaching the new ground state is transferred on the photoelectron (see Fig. 5.13(b)). This increases the

relation is denoted by

$$N \left(\frac{|o_1|}{|a_1|} \times \frac{|o_2|}{|a_2|} \right) R\Theta \tag{7.5}$$

where $N =$"p" or "c" for primitive or centred cells, respectively, and Θ is the angle by which the $\mathbf{o}_i$ vectors have to be rotated with respect to the $\mathbf{a}_i$ (see Fig 7.6). The nomenclature of Woods has the advantage of simplicity. It is, however, not possible to describe all surface / adsorbate structures because the rotation angle might not be the same for both vectors. Some examples for the application of the Woods nomenclature

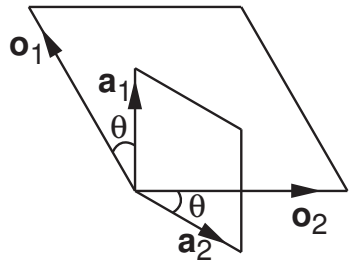

Figure 7.6: The Woods terminology for describing surface reconstructions and overlayers.

are given in Fig. 7.7. Note that despite of its lack of generality, the Woods nomenclature is still useful because many structures can be described by it.

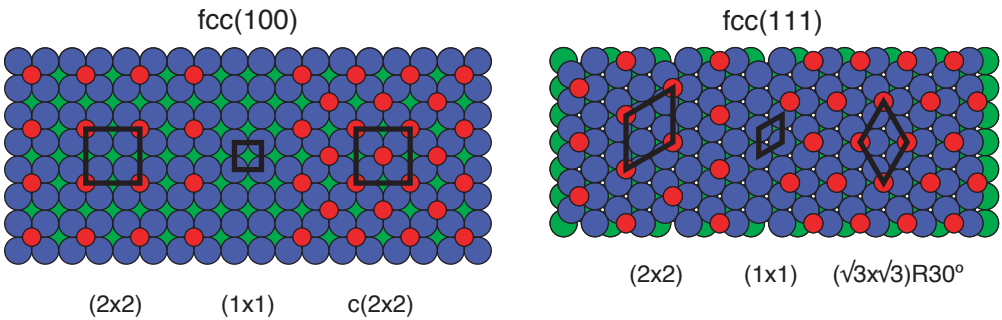

Figure 7.7: Examples for structures described by the Woods terminology.

A more general description of the surface structure is the so-called matrix notation . One writes

$$\begin{aligned} \mathbf{o_1} &= m_{11}\mathbf{a_1} + m_{12}\mathbf{a_2}, \\ \mathbf{o_2} &= m_{21}\mathbf{a_1} + m_{22}\mathbf{a_2}. \end{aligned} \tag{7.6}$$

or, equivalently,

$$\begin{pmatrix} \mathbf{o_1} \\ \mathbf{o_2} \end{pmatrix} = \begin{pmatrix} m_{11} & m_{12} \\ m_{21} & m_{22} \end{pmatrix} \begin{pmatrix} \mathbf{a_1} \\ \mathbf{a_2} \end{pmatrix}. \tag{7.7}$$

The description by a matrix is more complicated but all possible surface structures can be described. The inspection of the matrix elements directly allows the classification of the overlayer structures into the three types, illustrated in Fig. 7.8:

1. All the matrix elements are integer numbers: The surface / adsorbate and substrate lattices are called simply related and the combined Bravais lattice is the same as that of the surface / adsorbate.
2. Some matrix elements are rational: The surface / adsorbate and substrate lattices are called rationally related. The combined translational symmetry is given by the distance it takes before surface / adsorbate lattice and substrate lattice come into coincidence again.
3. Some matrix elements are irrational. In this case the surface / adsorbate lattice is incommensurate with the substrate, and no true lattice for the whole system exists.

It is obvious that the relative strength of the substrate-adsorbate and adsorbate-adsorbate interactions will favour one type of structure over the others.

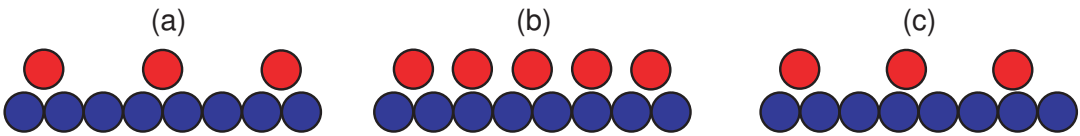

Figure 7.8: Types of overlayers. (a) The overlayer is simply related to the substrate. (b) The overlayer is rationally related to the substrate. (c) The overlayer and substrate lattices are incommensurate with no common periodicity between substrate and adsorbate lattice.

7.3 Low energy electron diffraction (LEED), LEED patterns and quantitative structure determination

Low-energy electrons are for surface structure what x-rays are for bulk crystal structure. We already know the two reasons for this: (1) the inelastic mean free path for low energy electrons in solids is short and therefore any technique based on such electrons is rather

surface sensitive and (2) for low kinetic energies, the electron de Broglie wavelength $\lambda_e = h/p$ is similar to typical distances in crystals and thus diffraction phenomena are to be expected. The discovery of the electron's wave nature was a milestone in the development of modern physics and actually achieved by an experiment that would be classified as LEED today. It was the diffraction of electrons from a nickel single-crystal by Davisson and Germer in 1927.

The quantitative structure determination with electrons instead of x-rays is unfortunately more difficult, because the electrons interact with the solid much more strongly than x-rays. This results in a refraction of the electron wave at the crystal-vacuum boundary and, even worse, it leads to a high degree of multiple scattering, such that the usual approximation of kinematic scattering has to be abandoned.

As we shall see below, there are two major applications for LEED. The first is to learn something from the pure inspection of the surface diffraction pattern. This gives immediate and direct information about the surface order and quality. When the surface is reconstructed or covered with an ordered adsorbate layer, the LEED pattern can quickly give some information about the surface symmetry and periodicities. The second application of LEED is the quantitative structure determination. This is more difficult. One has to measure the diffraction intensities as a function of the electron kinetic energy and compare them to sophisticated multiple-scattering calculations for a model system. This model system has to be changed until good agreement between calculated and measured intensities is achieved. Despite of this complicated procedure, LEED is the most important tool for quantitative surface structure determination.

7.3.1 Instrumentation

Fig. 7.9 shows a typical LEED apparatus that can be found in almost every surface science vacuum chamber. The LEED system has two major components: (1) an electron gun producing a beam of monochromatic electrons and (2) a detector system that detects only the elastically scattered electrons.

We already know how the electron gun works from Chapter 5. The detector consists of four metal grids at different voltages and a fluorescent screen. The first grid (counted from the sample) is on ground potential to ensure a field-free region around the sample. The next two grids are set to the so-called retarding voltage. This voltage is slightly lower than the kinetic energy of the electrons produced by the gun. It repels almost all the inelastically scattered electrons. The elastically scattered electrons pass the next grid which is set to ground potential again and are then accelerated towards the fluorescent

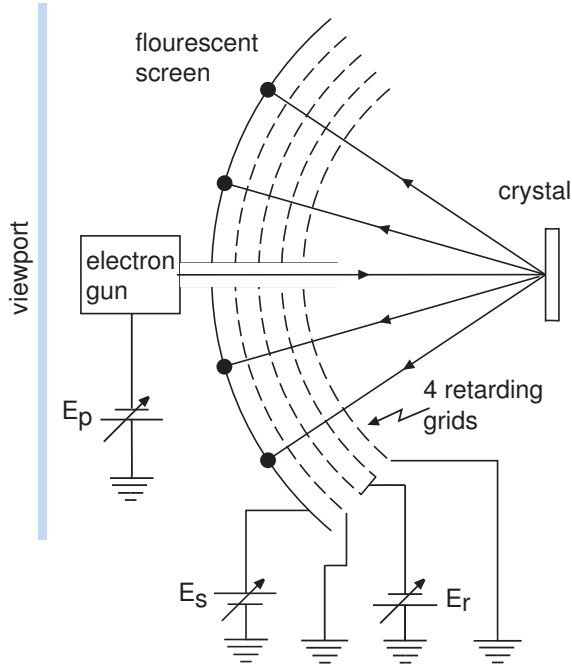

Figure 7.9: A LEED system.

screen which is set to a high positive voltage. Elastically scattered electrons hitting the screen give rise to light emission that is intense enough to be observed by the naked eye. Behind the screen there is a viewport in the vacuum system so that the LEED pattern can be observed directly or recorded with a camera.

7.3.2 LEED diffraction pattern and their analysis

While a surface is somewhat between being two-dimensional and three-dimensional, we start with the assumption of a purely two-dimensional case. The discussion of diffraction from a two-dimensional lattice is very similar to that of a three dimensional crystal. We will therefore only give a very short overview and not derive the conditions for constructive interference. The derivation is exactly the same as for x-ray diffraction from a three-dimensional crystal.
The diffraction conditions for a two-dimensional lattice are given by the Laue conditions

$$(\mathbf{k}_s^{\parallel} - \mathbf{k}_i^{\parallel}) = \Delta\mathbf{k}^{\parallel} = \mathbf{g}, \tag{7.8}$$

where $\mathbf{k}_i^{\parallel}$ and $\mathbf{k}_s^{\parallel}$ are the components of the incident ($\mathbf{k}_i$) and scattered ($\mathbf{k}_s$) electron wave vectors parallel to the surface and $\mathbf{g}$ is a surface reciprocal lattice vector.
What about the third component of the electron's wave vector, the one perpendicular to the surface, i.e. $k_i^{\perp}$ and $k_s^{\perp}$? So far, these did not enter the discussion because the surface lattice is only two-dimensional. For x-ray diffraction, there would be a third Laue condition but for LEED there is not, because the introduction of the surface has destroyed the periodicity of the solid in the direction perpendicular to it.
A condition for the vertical components $k_i^{\perp}$ and $k_s^{\perp}$ does, however, exist because of the requirement of elastic scattering. Energy conservation implies that the wave vectors have to have the same length, i.e.

$$|\mathbf{k}_s| = |\mathbf{k}_i|. \tag{7.9}$$

These two conditions can be illustrated by changing the Ewald construction familiar from x-ray scattering to the surface case. The bulk situation is shown in Fig. 7.10(a): We draw a $\mathbf{k}_i$-vector that ends at the origin of the reciprocal lattice and has the right length and direction corresponding to our experimental setup. Then we draw a circle of radius $|\mathbf{k}_i|$ around the starting point of the vector. The intersection of this circle and the reciprocal lattice points gives the possible final $\mathbf{k}_s$ vectors, for which we observe constructive interference. This construction ensures both that $\Delta\mathbf{k} = \mathbf{g}$ and that $|\mathbf{k}_s| = |\mathbf{k}_i|$ because of the circle.
For the surface case, there is no Laue condition perpendicular to the surface and this is taken into account by replacing the discrete points in the Ewald construction by rods perpendicular to the surface. To justify this, we could argue that the real-space periodicity in the third dimension is infinite, which means that the reciprocal lattice points have to be infinitely close to each other, forming the rods. Now we expect constructive interference whenever a rod intersects the sphere. Note that this is always going to happen for a sphere of sufficient size, i.e. a sufficiently high electron energy. It is evident that we will see many more spots in the two-dimensional case than in the three-dimensional case because the sphere does not have to hit points in k-space, it just has to intersect with the rods.
We now apply theses concepts to the real LEED experiment. In most cases, the sample in the LEED setup shown in Fig. 7.9 is oriented such that the electron beam hits the surface at normal incidence, i.e. such that $\mathbf{k}_i^{\parallel} = 0$. This greatly simplifies the analysis of the diffraction patterns because the diffraction maxima can be directly associated with the surface reciprocal lattice. In fact, according to (7.8) we obtain that $\mathbf{k}_s^{\parallel} = \mathbf{g}$ so that the diffraction pattern directly shows the surface reciprocal lattice.

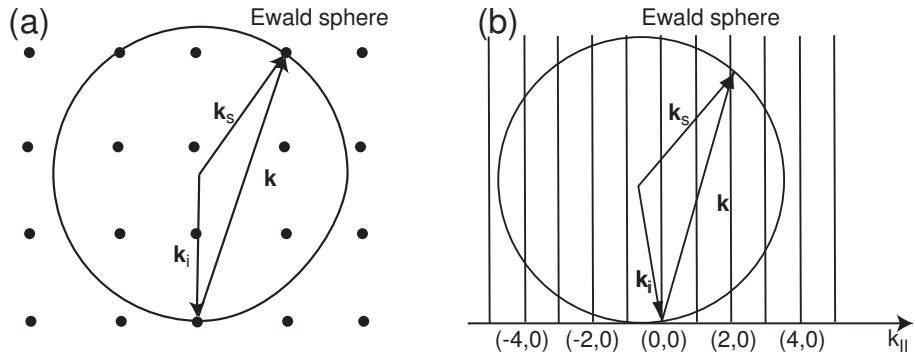

Figure 7.10: The Ewald construction for (a) the bulk case and (b) the surface case.

We also know the magnitude $|\mathbf{k}_s|$ of the scattering electrons and with this we can calculate the emission angle Θ_{hk} for a beam corresponding to the surface reciprocal lattice vector $\mathbf{g} = h\mathbf{b}_1 + k\mathbf{b}_2$ from $\sin\Theta_{hk} = |\mathbf{g}|/|\mathbf{k}_s|$. Consider the imaging by the LEED apparatus (Fig. 7.11). The position of the diffraction maxima on the viewport (the distance from the centre axis) is given by

$$d_{hk} = R\sin\Theta_{hk} = \frac{R}{|\mathbf{k}_s|}|h\mathbf{b}_1 + k\mathbf{b}_2| = R\frac{\hbar}{\sqrt{2m_e}}\frac{1}{\sqrt{E}}|h\mathbf{b}_1 + k\mathbf{b}_2|, \tag{7.10}$$

where R is the radius of the screen and E the kinetic energy of the electrons.

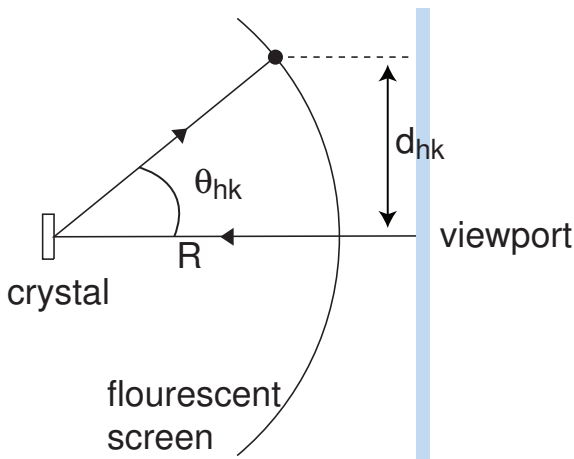

Figure 7.11: Imaging of the reciprocal lattice by LEED.

From equation. (7.10) we can see what happens when we change the kinetic energy of

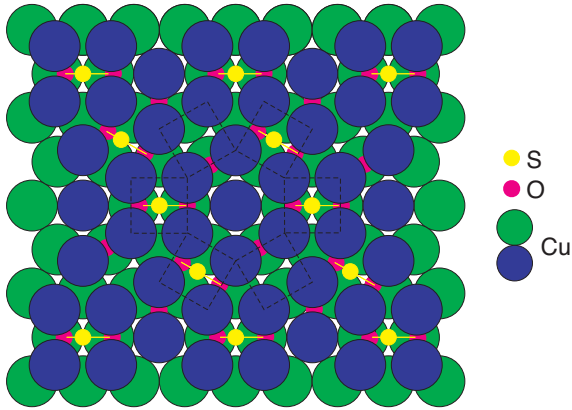

Figure 7.27: Structure SO_2 + O on Cu(111) as determined by SEXAFS. After ref. [32].

extended π^* state. If we excite electrons from a core level, e.g. the N $1s$ state close to the adsorption edge, we expect a strong maximum in the absorption cross section when we hit the photon energy at which the $1s$ electron can be excited into an unoccupied molecular orbital, such as the LUMO, the LUMO+1 and so on.
Observing this enhancement is already very useful as such, because it gives us the energy position of the unoccupied states of a system. However, the approach can also be used to extract further geometrical information, for example about the orientation of the adsorbed molecules. To see this, consider again the dipole selection rule for an s electron as an initial state. The outgoing electron wave has p symmetry and is oriented in the direction of the light's polarisation vector. The matrix element for the excitation into an unoccupied molecular orbital is now calculated between this p wave and the wave function of the orbital. Consider the situation in Fig. 7.28(b) and (c) where the polarisation of the light is chosen such that the resulting p wave is perpendicular to the plane of the molecule. If the unoccupied molecular orbital has σ^* character, the matrix element has to vanish because the product of the σ and the p waves "above" the molecular plane is the same as "below" the plane, apart from the sign difference in the p wave. Therefore, this particular excitation is only possible for a molecular orbital of π character. Similar arguments can be made for the light polarisation vector parallel to the plane of the molecule. In this case, only an excitation into orbitals of σ symmetry is possible. Thus, the absorption due to a particular orbital will strongly depend on the orientation of the molecule with respect to the polarisation vector of the light. If the molecules are oriented by the surface, a different light polarisation need to be chosen to achieve the excitation into a given orbital type.

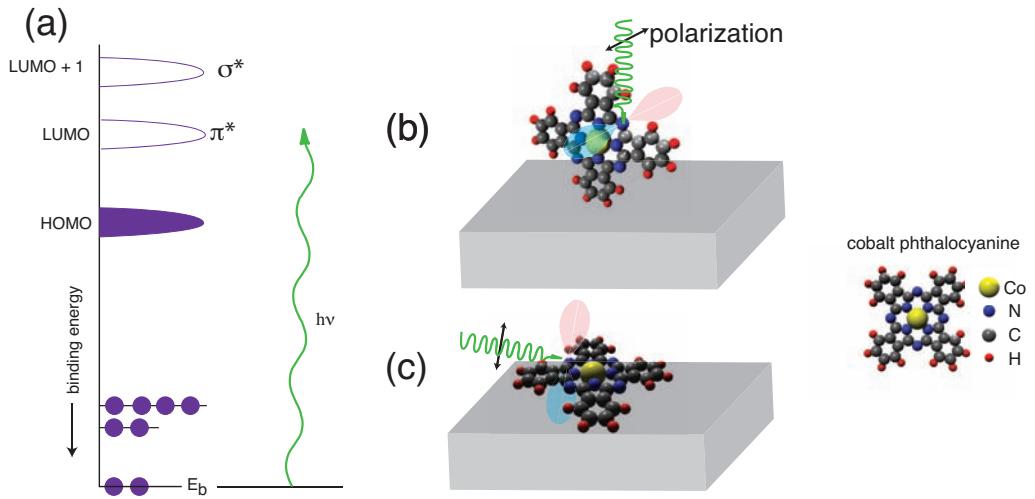

Figure 7.28: Illustration of the NEXAFS phenomenon. (a) Occupied (filled) and unoccupied (empty) states for a molecule adsorbed on a surface, including core levels and molecular orbitals. A strong adsorption can be expected when a core electron can be photoexcited into an unoccupied molecular orbital. (b) and (c) When exciting the N $1s$ core level of the Co-phthalocyanine molecule (sketch at the side), the dipole selection rules dictate the outgoing electron wave to have p character. Excitation into the unoccupied π^* LUMO is only possible when the light polarisation vector is perpendicular to the molecular plane. This can be used to determine the orientation of the plane with respect to the surface.

This can be exploited in order to determine the molecular orientation with respect to the surface, as illustrated in Fig. 7.29, again using the example of cobalt phthalocyanine. Shown is a set of NEXAFS absorption spectra near the nitrogen K-edge. From the known electronic structure of the molecule, the series of peaks closest to the edge are assigned to transitions into orbitals of π^* symmetry, whereas the broader peaks further away from the edge are due to transition into σ^* states. As the angle between light incidence and surface normal Θ is changed, drastic intensity variations in the absorption spectrum are observed. For Θ closest to 0° (90°) the intensity of the σ^* (π^*) states is highest. Since the polarisation vector of the light is perpendicular to the light propagation direction, we can directly conclude from this that the molecule is absorbed with the molecular plane parallel to the surface.

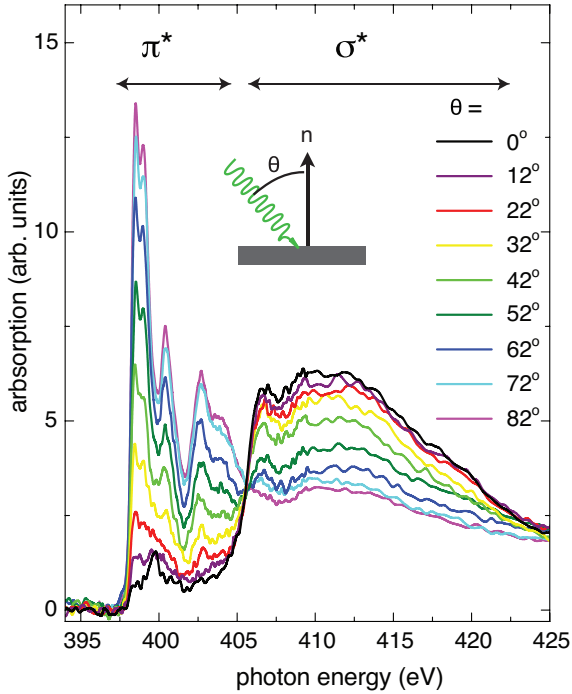

Figure 7.29: NEXAFS data do determine the orientation of the molecular plane of adsorbed Co phthalocyanine. After [33].

7.7 Photoelectron diffraction (PhD, PED)

7.7.1 Introduction

Photoelectron diffraction is yet another structural technique that is particularly well suited to determine the structure of adsorbates on a surface. The principle is illustrated in Fig. 7.30. Consider the emission of a core level electron from an atom adsorbed on a surface, as in a typical XPS experiment. In our discussion of XPS, we had described the final state wave function as an outgoing wave with a symmetry given by the dipole selection rules (e.g. a p wave for and s initial state). As in EXAFS, the effect of photoelectron diffraction can only be understood if we acknowledge that this final state is actually more complicated. A convenient way to think about the final state is as follows: Consider a detector that measures the photoemission intensity of the adsorbate core level in a certain direction. There are many possibilities for the photoelectron to

exerted on the tip and this leads to a small deflection of the cantilever. The deflection can be measured optically, for example by reflecting a laser beam from the cantilever and tracking the motion of the reflected light spot. Then this deflection can be measured as a function of the x and y coordinates parallel to the surface, in the same way as for the STM.

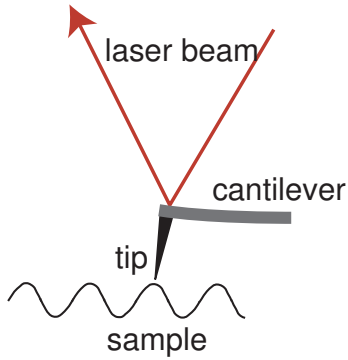

Figure 7.48: Principle of the atomic force microscope. An atomically sharp tip is mounted at the apex of a flexible cantilever. As it is moved across the surface, the force between the surface atoms and the tip leads to a deflection of the cantilever and this can be measured by the reflection of a laser beam.

While this approach to AFM is certainly possible, it is not the method of choice in order to achieve atomic resolution. For this, so-called dynamic AFM is used. The experimental setup for this is essentially identical to what is shown in Fig. 7.48, apart from an additional modification needed to excite the cantilever to vibrate at a certain frequency. This can be done by coupling a magnetic cantilever to an electromagnet or by inducing a vibration via mechanical coupling to a vibrating piezoelectric crystal. The vibrating cantilever is then brought close to the surface, so that it starts to "feel" the force between the tip and the atoms on the surface. Even if the vibrational amplitude is chosen so large that the cantilever tip is only close to the surface for a small fraction of the vibrational cycle, this can be enough to make the tip-surface interaction detectable. This interaction leads to two changes in the forced vibration: a change in amplitude and a change in resonance frequency.
We discuss a simple model to illustrate this. The model is, in fact, far too simple to give even a qualitative agreement with experiment but it illustrates the basic physical principle behind dynamic AFM. We describe the motion of the entire cantilever as a vibration of a harmonic oscillator with an effective mass m. The oscillator is driven by

an external harmonic force of amplitude F_{ext} and frequency ω. It has a force constant γ_c and, in the absence of damping, a resonance frequency $\omega_0 = (\gamma_c/m)^{0.5}$. Finally there is a damping that is proportional to the velocity. The damping is quantified by the so-called quality factor Q. This is a dimensionless number. The higher Q, the smaller the damping. The equation of motion is then

$$m\frac{d^2z}{dt^2} + \frac{m\omega_0}{Q}\frac{dz}{dt} + m\omega_0^2 z = F_{ext}\cos\omega t, \tag{7.22}$$

After some transient time, the steady state solution of this problem is that the oscillator follows the externally imposed frequency ω, i.e. that

$$z(t) = A\cos(\omega t - \phi), \tag{7.23}$$

with A being the (real) amplitude of the oscillation and ϕ the phase difference between the motion of the oscillator and the external excitation. For the amplitude one finds

$$A = \frac{F_{ext}/m}{\sqrt{(\omega_0^2 - \omega^2)^2 + (\omega\omega_0/Q)^2}}. \tag{7.24}$$

From this we see that resonance in the absence of damping (Q very large) is achieved when $\omega = \omega_0$. The existence of damping slightly changes the resonance frequency. By taking the derivative of (7.24) with respect to ω one finds that the resonance frequency in the presence of damping is

$$\omega_0' = \omega_0\sqrt{1 - \frac{1}{2Q^2}}. \tag{7.25}$$

For the cantilevers used in AFM $Q \approx 10^4$, implying that the damping is sufficiently small to ignore the difference between ω_0' and ω_0. When the excitation frequency is changed and the amplitude is monitored, a resonance curve as in Fig. 7.49 is obtained.
What happens now if we bring the vibrating cantilever close to the surface? It is easy enough to modify the equation of motion such that it includes the tip-surface interaction $F_{ts}(z)$

$$m\frac{d^2z}{dt^2} + m\omega_0^2 z + \frac{m\omega_0}{Q}\frac{dz}{dt} = F_{ts}(z) + F_{ext}\cos\omega t, \tag{7.26}$$

but the trouble with solving this equation is that vibrational amplitude of the cantilever can be quite big in AFM ($A > 10$ nm), so that the tip spends only a small fraction of

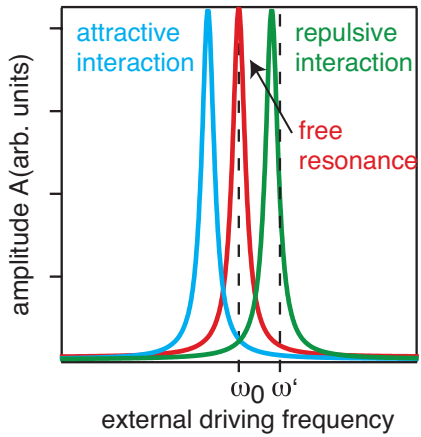

Figure 7.49: Resonance curves for a free AFM cantilever and a cantilever in the presence of an attractive / repulsive tip-surface interaction.

the cycle close to the atoms of the surface and $F_{ts}(z)$ varies dramatically over one cycle. Moreover, $F_{ts}(z)$ is not known and several types of forces contribute to it.
In order to illustrate the key-idea of dynamic AFM, however, we make the (invalid) assumption that $F_{ts}(z)$ can be linearized for the motion of the cantilever. Then, we can readily determine the new resonance frequency of the cantilever by combining the force constant of the free cantilever with that due to the tip-surface interaction

$$F_{eff} = -m\omega_0^2 z + F_{ts}(z) = -(\gamma_c + \gamma_{ts})z, \tag{7.27}$$

giving

$$\omega = \sqrt{\frac{k}{m}} = \sqrt{\frac{\gamma_c + \gamma_{ts}}{m}}. \tag{7.28}$$

If we assume that $\gamma_c \gg \gamma_{ts}$, we can expand the vibrational frequency as

$$\omega(\gamma_c + \gamma_{ts}) = \omega(\gamma_c) + \frac{d}{d\gamma}\omega(\gamma_c)\gamma_{ts} + ... \tag{7.29}$$

and finally obtain

$$\omega(\gamma_c + \gamma_{ts}) \approx \omega_0 + \frac{1}{m}\frac{1}{2\sqrt{\gamma_c/m}}\gamma_{ts} = \omega_0 + \frac{\gamma_c}{m}\frac{1}{2\sqrt{\gamma_c/m}}\frac{\gamma_{ts}}{\gamma_c} = \omega_0 + \frac{\omega_0\gamma_{ts}}{2\gamma_c}. \tag{7.30}$$

The frequency shift depends on the ratio between γ_{ts} and γ_c and on the sign of γ_{ts} for attractive and repulsive interactions. Is there any hope to measure it? Let us assume that γ_{ts} is of the order of a typical interatomic force constant in a solid, something we can get out of Young's modulus or the typical vibrational frequencies. This gives $\gamma_{ts} \approx 1$ Nm^{-1} (very approximate). The force constant of a typical cantilever is $\gamma_c \approx 10$ Nm^{-1} and since frequencies can be measured very precisely, detecting the resulting shift is quite possible.

In practice, dynamic AFM experiments use two different strategies. The first tracks the local resonance frequency, as the tip is moved across the surface. This is done using a clever feedback mechanism rather than measuring a resonance curve for every point of an image. The frequency shift can then be used as an image of the surface topography. This mode of dynamic AFM is called frequency modulation AFM or sometimes also non-contact AFM. It is the preferred mode for UHV experiments aiming at high resolution. Using this mode of AFM, it has been possible to obtain atomically resolved images of many insulator and semiconductor surfaces, among others Si(111)(7×7), something that had long been an elusive goal in AFM [45].

An example of this is given in Fig. 7.50 that shows both non-contact AFM and STM images of the TiO_2(110) surface. The surface structure of TiO_2(110) is sketched in Fig. 7.50(a). It is terminated by rows of oxygen atoms and these rows are clearly visible in the AFM image of Fig. 7.50(b), along with a weaker corrugation along the rows. The surface shows prominent defects on the rows and these have been identified as single hydrogen atoms, forming an OH group with the topmost oxygen atom. The STM image in Fig. 7.50(c) has been taken simultaneously with the AFM image. In contrast to all other STM images in this book, it is not a constant current image but just a measurement of the tunnelling current through the conductive AFM tip as it is moved along the surface. The image shows the atomic corrugation along the rows even clearer than the AFM image. The OH groups, on the other hand, are imaged less prominently than in the AFM image. At first glance, it is quite surprising that taking any kind of STM image is at all possible because TiO_2 has a band gap of more than 3 eV and is thus too insulting for electron spectroscopy. It turns out, however, that TiO_2 crystals can be heavily doped by heating in vacuum, a process that creates oxygen vacancies. This is commonly done to allow electron spectroscopy on this material. For an intrinsic TiO_2, the STM image in (c) could not have been taken but the AFM image could.

Another approach to dynamic AFM is to excite the cantilever with a fixed frequency ω and to monitor the changes in the vibrational amplitude, as the tip approaches the sample. This technique is called amplitude modulation AFM. We can see how the

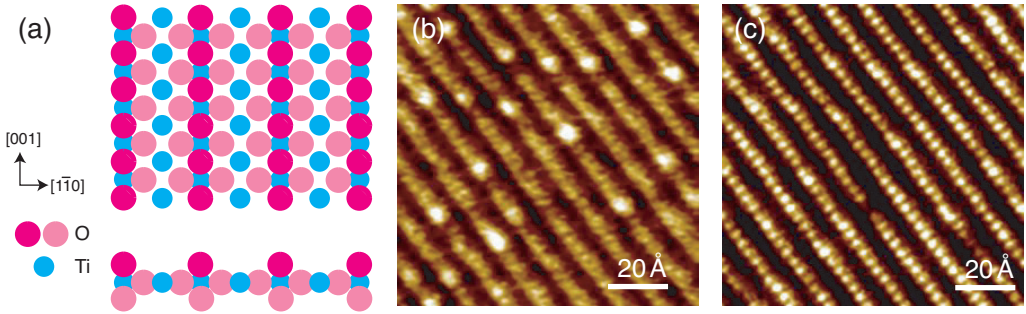

Figure 7.50: (a) Structure of the TiO_2(110) surface. (b) Non-contact AFM image. (c) Tunnelling current measured during the acquisition of the AFM image. After [46].

presence of the surface would affect the amplitude by inspecting the resonance curves in Fig. 7.49. If we excite the cantilever with the free resonance frequency ω_0 and the tip-surface interaction shifts the resonance curve, we would obtain a smaller amplitude, no matter if the tip-surface interaction is attractive or repulsive. We could actually also distinguish between attractive and repulsive tip-surface interactions by exciting the cantilever slightly off its resonance frequency, at ω'. In this case, a repulsive interaction would increase the observed amplitude whereas an attractive interaction would decrease it. Amplitude modulation AFM is frequently used in air and in water to obtain high resolution. Note again, that the picture of a constant tip-surface force constant is a strong oversimplification. Even the sign of the force can change in one cycle.

7.10 Further reading

For a more detailed discussion of surface thermodynamics, consult the general surface physics books listed in the Preface. For the basics of surface structure, consider especially the book by Woodruff and Delchar. Details on LEED can be found in

- Low energy electron diffraction by J. B. Pendry, Academic Press, 1974.
- Low energy electron diffraction by M. Van Hove, W. H. Weinberg and C. M. Chan, Springer, 1986.

For photoelectron diffraction, see

- Photoelectron diffraction by D. P. Woodruff in Angle Resolved Photoemission, ed. S. D. Kevan, Elsevier, 1992.

For x-ray absorption techniques, also consider the book by Woodruff and Delchar and

- NEXAFS Spectroscopy by J. Stöhr, Springer 2010.

For STM and AFM, see

- Scanning Probe Microscopy and Spectroscopy: Methods and Applications by R. Wiesendanger, Cambridge University Press, 1994.

7.11 Discussion and Problems

Discussion

1. Explain the phenomena of surface relaxation and reconstruction and their physical origin.
2. Explain the Woods and matrix nomenclatures for surface reconstructions and ordered overlayers and discuss their advantages and restrictions.
3. Explain how the technique of low-energy electron diffraction (LEED) works experimentally.
4. Discuss what the inspection of a LEED diffraction pattern can tell you about the structure of a surface under investigation. What type of information is not readily obtained from a mere inspection of the LEED pattern?
5. What is the reason for the strong intensity variations observed in LEED I-V curves?
6. How can LEED be used to determine surface structures quantitatively, e.g. in order to find the precise position of adsorbed atoms within the surface unit cell.
7. Explain the basic idea behind x-ray absorption techniques such as NEXAFS, EXAFS and SEXAFS. What can be learned from these experiments?
8. Explain the basic idea behind photoelectron diffraction. How can this phenomenon be used for surface structure determination.
9. Explain the working principle of a scanning tunnelling microscope (STM), especially how imaging in the constant current mode works.
10. How does the tunnelling current in STM depend on the tip-sample distance and why?
11. What is the physical interpretation of a constant current mode STM image measured with a very small bias voltage?
12. Explain the working principle of an atomic force microscope (AFM).
13. Discuss the differences between STM and AFM and the samples these techniques can be used on.

Problems

1. *LEED:* Fig. 7.13 shows the energy dependence of the (0,0) spot of Ni(100). In practice this means that you have to measure the normal incidence reflectivity of the crystal for electrons. How would you do this? (This is a tricky question, if you lack the right idea for an answer, simply ignore this and go on). The finite width of the LEED I/V peaks is caused by two effects: (1) Electron waves that fulfil the Bragg-condition in a perfect crystal will eventually get totally reflected (therefore band gaps open at the Brillouin zone boundary when a potential is present). This leads to a limited number of scatterers producing the I/V peaks and therefore to a finite width of the peak. (2) The limited mean free path of the electrons in the sample also leads to a finite width of the peaks. Make a very simple estimate of the penetration depth of the electrons from the peak width. Hint: calculate the Δk corresponding to the peak width ΔE and use the uncertainty principle.
2. *LEED:* The measurement and analysis of the (-2,1), (0,-2) and (0,2) beams if Fig. 7.17 starts at a rather high energy. Why? Hint: Consider that the measurement is practically done by tracking the spots on the LEED screen.
3. *LEED:* Draw a possible structural model and the LEED pattern for
   - Cu(001)($\sqrt{2} \times \sqrt{2}$)R45°-O
   - Cu(001)($\sqrt{2} \times 2\sqrt{2}$)R45°-O
   - Cu(111)($\sqrt{3} \times \sqrt{3}$)R30°-O

   For the first two structures, are there notations that avoid the roots?
4. *Surface reconstructions:* Show that a

$$\begin{pmatrix} 22 & 0 \\ -1 & 2 \end{pmatrix} \tag{7.31}$$

   reconstruction on Au(111) does in fact give rise to a rectangular unit cell as shown in Fig. 7.42(b).
5. *Surface overlayers:* (a) Discuss in general how the relative strength of adsorbate-adsorbate and adsorbate-substrate interactions can be expected to determine if an adsorbate overlayer is simply related, rationally related or incommensurate with the substrate. (b) Discuss the specific example of graphene on transition metal surfaces.
6. *STM:* Assuming a small tunnelling voltage and the validity of the Tersoff and Hamann model for the interpretation of STM images taken in the constant current mode, we have argued that the Cl atoms on jellium would not be detectable by STM (see Fig. 6.7). Speculate how the appearance of the Cl atoms might change

as you increase the tunnelling voltage, going either to positive or to negative bias voltages.

7. *STM:* The oxygen-induced rows of the reconstruction appear to be well-resolved in the STM images of Fig. 7.45 but the step edges on the surface are quite fuzzy. Give a plausible explanation for this.
8. *STM:* Some adsorbates can be seen by STM experiments at low temperatures but not at higher temperatures, even though other techniques (name a possible technique) clearly indicate that the adsorbates are neither desorbed or dissolved in the bulk. Discuss how this can be possible.
9. *Surface structure determination:* Compare the different techniques for surface structure determination presented in this Chapter, comparing their restrictions and advantages.

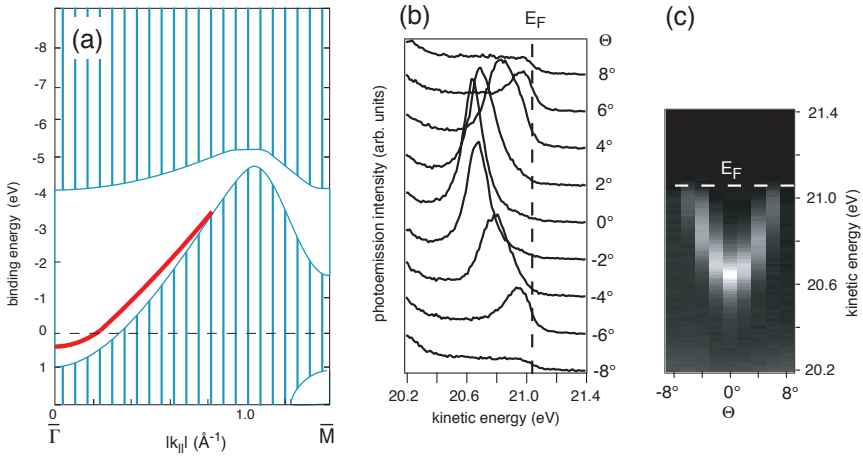

Figure 8.16: Surface state dispersion on Cu(111). (a) Projected bulk band structure of Cu(111) (hatched blue area) with the surface state dispersion in red. (b) ARPES spectra taken at different emission angles close to the surface normal direction. (c) Grey-scale image of the same data.

parabolas shifted against each other along $k_{\|}$ [55], such that their crossing point at $k_{\|} = 0$ is no more the point with the highest binding energy. It is tempting to believe that the splitting between the bands is somehow related to the complex herringbone reconstruction on Au(111) (see Fig. 7.42) that is absent for Cu(111). However, the effect of the reconstruction on the surface state dispersion is only very small and the splitting is caused by an altogether different effect, the spin-orbit interaction, that is much stronger in heavy metal gold than in copper. Indeed, using higher resolution still a much smaller spitting of the same kind can also be observed for the Cu(111) surface state [56].

The spin-orbit interaction is a relativistic effect known from the splitting of core levels in atoms with $l \neq 0$. For deep core levels in heavy atoms, where the electron speed near the nucleus can approach the speed of light, the splitting can be quite strong and we have seen that a splitting of several electron volts is observed, even for the shallow core levels of the heavy element bismuth (Fig. 5.9). For valence electrons one would expect the splitting to be smaller but here it is still observable. In the special case of a two-dimensional electron system, such as a surface state, a spin-orbit splitting can be caused by an electric field perpendicular to the plane the electrons move in. We know that there is such a field near the surface of a metal because of the quite general effect

of an electron spill-out discussed in connection with Fig. 2.10. For a free electron-like two-dimensional state in the presence of such an electric field, the modification of the dispersion due to spin-orbit splitting has been predicted by Rashba to be

$$E(k) = \frac{\hbar^2 k^2}{2m_e} \pm \alpha \hbar k. \tag{8.20}$$

The first term is the kinetic energy of the free electron and the second term is the correction due to the spin-orbit interaction. The $\pm$ sign stands for the two different spin directions of the electrons and α is a scaling parameter that, among other things, includes the strength of the electric field perpendicular to the plane of the surface. Fig. 8.17(b) and (c) show this resulting dispersion for free electrons without spin-orbit interaction ($\alpha = 0$) and a finite α, respectively. We see that a finite α splits the band into two branches with binding energy maxima moved away from $k = 0$, as expected by re-writing (8.20) as

$$E(k) = \frac{\hbar^2}{2m_e} \left(k \pm \frac{\alpha m_e}{\hbar^2} \right)^2 - \frac{\alpha^2 m_e}{2\hbar^2}, \tag{8.21}$$

and in perfect agreement with the data from the Au(111) surface state. It is interesting to note that the splitting lifts the spin-degeneracy of the state. Whereas a "normal" band in a solid can accommodate two electrons per k value, one for each spin direction, this degeneracy has been lifted in the Rashba model, except for the band crossing at $k = 0$. The states are spin-split and the direction of the spin is indicated by arrows in Fig. 8.17(c).

It is easy to come to a qualitative understanding of the Rashba-type spin-orbit splitting. Suppose that an electron moves in the plane of the surface and that the electric field is perpendicular to the surface. The electron experiences the Lorentz-transformed electric field as a magnetic field that is also lying in the surface but perpendicular to the k vector of the electron. Now the electron's energy depends on the orientation of its spin with respect to this magnetic field (parallel or anti-parallel) and this causes the splitting. The splitting increases with the magnitude of k because the kinetic energy does.

While the Shockley states appear in the nearly free electron model, one can also approach the question of surface states from the opposite viewpoint, namely in a tight-binding picture. There the atomic orbitals that stick into the vacuum because the atoms' neighbours have been cut off, have very different electronic properties than the equivalent bulk orbitals and represent surface localised states. This kind of more localised surface state is called a Tamm state. Examples of Tamm states can also be found on metals. One is a surface state which is derived from the Cu(001) d-band and shown in Fig. 8.18.

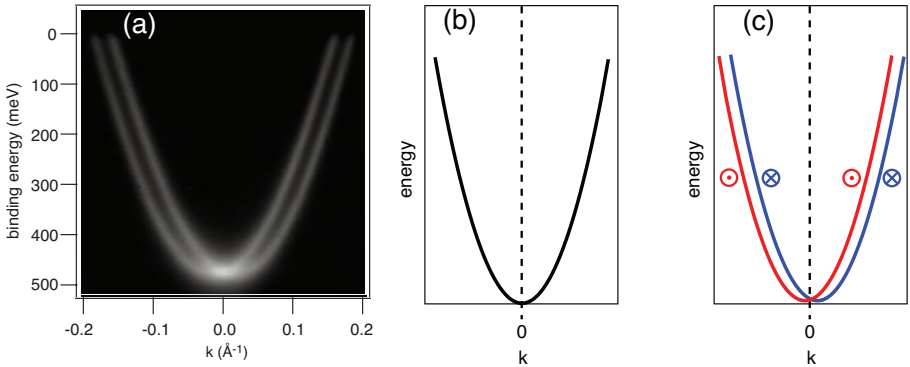

Figure 8.17: (a) Measured surface state dispersion on Au(111) (photoemission intensity) from Ref. [57]. (b) Free electron dispersion (Rashba model with $\alpha = 0$). (c) Rashba model with $\alpha \neq 0$. The spin-degeneracy is lifted and the spin direction is indicated by the arrows pointing into and out of the plane of the paper.

In the end of the day, the distinction between Shockley states and Tamm states is, of course, somewhat artificial, as it does not make any difference which simple model is used to explain the existence of surface states.

Adsorbate-covered metal surfaces

Angle resolved photoemission can also be used to probe the modification to the surface electronic structure that is induced by adsorption. Adsorption can modify the existing surface states. Alkali atom adsorption, for example, can lead to a "filling" of the existing surface states on the noble metals, increasing the occupied band width, consistent with the picture of electron donation by alkali atoms to the surface shown in Figs. 6.7 and 6.8. When adsorbing atoms or molecules on the surface, their orbitals can also give rise to additional surface-localised features in the electronic structure. We give three examples here.

Fig. 8.19 shows two spectra taken from CO adsorbed on Ni(001). Both are taken in normal emission but the direction of the incoming light and hence the polarisation vector is different. The spectra show peaks that are not present for the clean surface and thus assigned to the molecular orbitals of CO. A comparison with the energy of the peaks from gas phase CO leads to an identification of the higher binding energy peak as stemming from the 4σ orbital and the lower binding energy peak from both the 1π and 5σ orbitals. When the polarisation vector is parallel to the surface, the 4σ peak is not

then $\cosh k_i a > 1$ and we get a new solution as indicated by the red curve on the top of the optical branch in Fig. 9.1. This means that we can have new surface-localised solutions above the continuum of bulk states.
The other possibility for a real $\cos(k_r a + i k_i a)$ appears at the Brillouin zone boundary $(k_r = \pi/a)$ because there $\sin k_r a = 0$. Now (9.1) is reduced to

$$\omega^2 = \gamma M_R^{-1} \pm \gamma \left[M_R^{-2} - \frac{2}{M_1 M_2} (1 + \cosh k_i a) \right]^{1/2}, \tag{9.4}$$

i.e. like (9.3) but with a changed sign in front of the $\cosh$. If we choose $k_i = 0$ we get two different solutions corresponding to the highest frequency of the acoustic branch and the lowest frequency of the optical branch. If we choose $k_i > 0$, we get two real solutions following the red curve at the Brillouin zone boundary in Fig. 9.1. Because of the sign change in (9.4), there is now an upper limit for k_i that is given by the requirement to have a positive argument in the square root. The two solutions converge to one at the point where the square root is zero.

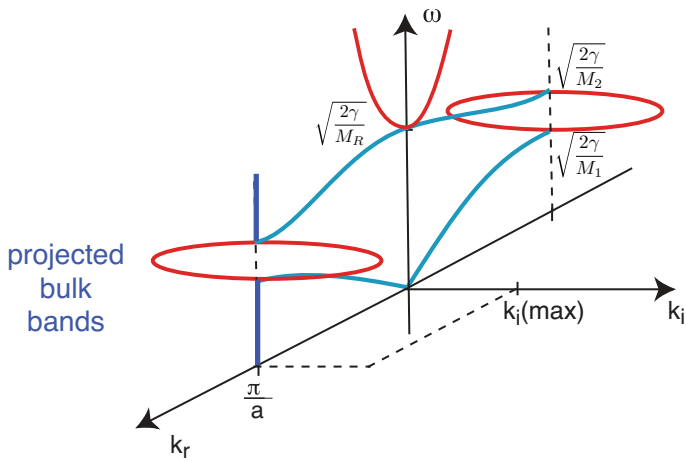

Figure 9.1: Phonon dispersion of a one-dimensional chain with two atoms per unit cell (blue). Chain-end localised solutions (red) are possible in the projected bulk band gaps at the Brillouin zone boundary and above the bulk continuum at the zone centre.

The simple model is thus giving us surface-localised vibrations in the projected bulk band gaps, as we have found in the case of the electronic surface states. The extension to two-dimensional surfaces is straight forward: As in the case of the electronic states, a necessary (but not sufficient) condition for the existence of a surface vibrational mode

is that this mode is placed in a projected band gap of the bulk vibrational spectrum. We illustrate this by an example. This time, we use the (0001) surface of the hcp metal beryllium. Fig. 9.2 shows the bulk phonon dispersion of beryllium, the bulk Brillouin zone and its projection onto the close-packed (0001) direction, giving the surface Brillouin zone. This projection is much simpler than any of those we had seen for the fcc Brillouin zone.

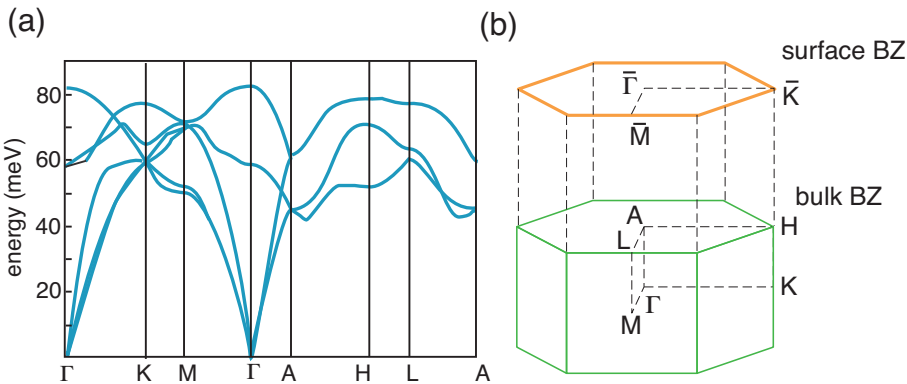

Figure 9.2: (a) Bulk Phonon dispersion of beryllium after Ref. [70]. (b) Bulk Brillouin zone (BZ) of beryllium (hcp structure) and surface Brillouin zone of Be(0001) obtained by projection.

Fig. 9.3 shows the projected bulk phonon dispersion for Be(0001) together with the surface phonon modes, calculated and measured. We can understand the projection of the bulk phonon structure from the dispersion in Fig. 9.2. Consider for example the $\bar{\Gamma}$ point, i.e. $\mathbf{k}_{\parallel} = (0,0)$. This corresponds to the bulk $\Gamma - A$ direction and an inspection of the dispersion in Fig. 9.2(a) shows that there is no projected band gap in this direction. In fact, since the acoustic mode of any material starts at Γ and $\omega = 0$, the bulk phonon continuum at a surface $\bar{\Gamma}$ will always start at zero. For the $\bar{M}$ point at the surface Brillouin boundary, we would have to consult the $M - L$ line. While this line is not given in the calculation of 9.2(a), both the M and the L points are present and the acoustic branches have reached an energy of more than 50 meV at both points. It is therefore fair to assume that there are no modes with a significantly lower energy along the $M - L$ line and that there is thus a large projected band gap for low energies. This is indeed found in the projected phonon bands of 9.3. In fact, "guessing" where the projected band gaps are is a lot easier for phonon bands than for electron bands because similar gaps at low energies are always likely to be found along lines connecting

points at the Brillouin zone boundary.
Fig. 9.3 also shows the dispersion of surface-localised vibrational modes. The filled red dots are calculated surface modes using the same force constants that give a good description of the bulk phonon dispersion and the open red symbols are the measured surface vibrational frequencies using electron energy loss spectroscopy, a technique we shall describe later. Clearly the agreement is not particularly good. The force-constants at the surface must be different from the bulk values.
A characteristic surface vibration is the lowest-lying acoustic mode that is split off the bulk continuum and most clearly visible at the surface Brillouin zone boundary near $\bar{M}$ and $\bar{K}$. This surface acoustic mode is called the Rayleigh wave, as it has first been predicted by Lord Rayleigh in 1885. It is found on many surfaces, including the surface of the earth where it plays an important role in the propagation of earthquakes. Interestingly, we see that the slope of the Rayleigh mode dispersion close to $\bar{\Gamma}$ is smaller than for any of the other projected acoustic modes. Also the highest energy of the Rayleigh mode is smaller than the lower edge of energies from the bulk vibrations. This is consistent with the simple picture of softer force constants, lower vibrational energies and a lower Debye temperature at the surface due to the missing neighbour atoms.

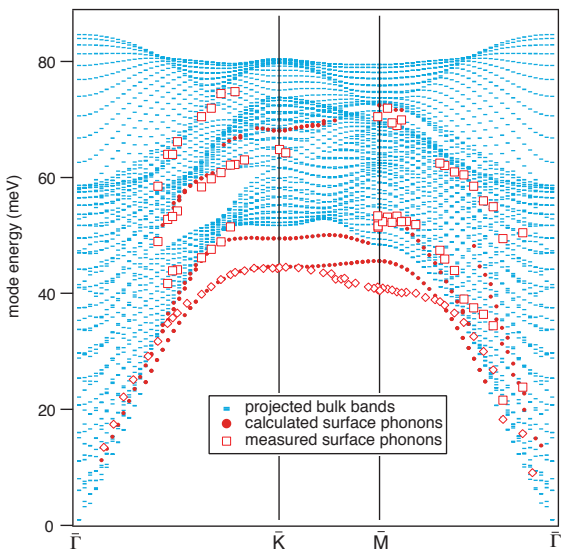

Figure 9.3: Bulk phonon dispersion of Be, projected onto the (0001) surface (blue dots). Calculated surface phonon dispersion for Be(0001), calculated from the bulk force constants (filled red markers) together with a measurement (open markers). After Ref. [71].

these curves is clear for a high k_x: The lower curve corresponds to the surface plasmon and the higher curve corresponds to light. At small k_x, however, it is no longer possible to make a clear distinction between light and the surface plasmon.
It is important to keep in mind that the k_x scale of this sketch is *very* small, much smaller than the typical size of the surface Brillouin zone. In fact, this is already clear because the Figure shows the light dispersion $\omega = ck_x$ clearly, in contrast to the graphs for the entire Brillouin zone, where this dispersion virtually coincides with the vertical axis of the graph.

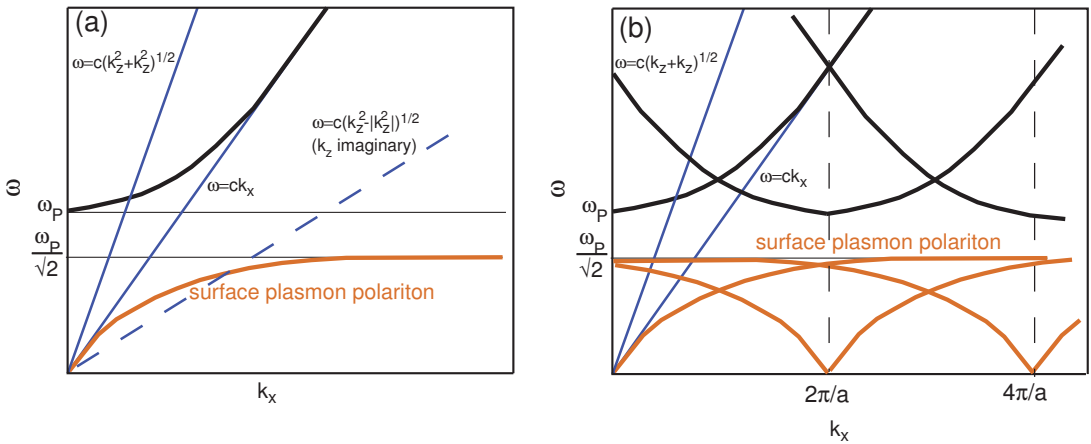

Figure 10.3: (a) Dispersion of a surface plasmon polariton. (b) Coupling the surface plasmon polariton to light be introducing a periodic structure on the surface.

As a consequence of the dispersion, it is impossible to excite surface plasmons with light because energy and momentum cannot be conserved simultaneously. This is easily seen from Fig. 10.3(a). The light dispersion line can be changed via the angle of incidence. For normal incidence $k_x = 0$ and the dispersion is a vertical line in the Figure. For grazing incidence $k_z \approx 0$ the dispersion is $\omega = ck_x$. For any angle in between, $\omega = c(k_x^2 + k_z^2)^{1/2}$. These curves are shown in Fig. 10.3(a) and it is evident that they never cross the surface plasmon polariton dispersion. The absence of a crossing implies that we cannot excite the plasmon by a photon while conserving both energy and momentum. Such a process would involve the annihilation of a photon with $(\hbar\omega, k)$ and the creation of a surface plasmon with the same $(\hbar\omega, k)$, i.e. it would be possible only if the two dispersion curves cross.
Exciting surface plasmons with light is very desirable. It would strongly couple the

light field to the surface and could therefore increase the surface-sensitivity of optical techniques. Surface plasmons are also confined to the surface, so if they could be launched with a light pulse, they could then propagate in a specially designed device. Indeed, for applications like this it would be an advantage that they cannot easily decay by light emission either. All this is possible, but the excitation is not straight-forward, as we have seen. There are essentially two ways of circumventing the lack of a crossing between the light dispersion line and the surface plasmon polariton. The first way to achieve a coupling is to use "slow" photons by using an imaginary k_z value. Then the dispersion line can be moved down, as indicated by the dashed line in Fig. 10.3(a). Such light can be produced by a total reflection inside a prism mounted at a short distance above the surface. In this case, an evanescent electric field penetrates the gap between prism and surface. The field decays exponentially, i.e. it possesses an imaginary k in the z direction.
Alternatively, one can fabricate a periodic structure on the surface, e.g. a grating or a regular array of holes. Suppose that this structure has the periodicity a, then its reciprocal unit cell has the periodicity $2\pi/a$. In such a periodic structure, k is only defined plus or minus a reciprocal lattice vector and the surface plasmon polariton branch starts not only at $k = 0$ but at every reciprocal lattice point. Now other branches cross the light dispersion lines, as sketched in Fig. 10.3(b). Since the k-scale for the dispersion is very small, so must be the reciprocal length $2\pi/a$. This is easy to achieve, since it means that the lattice constant of the artificial structure has to be fairly large (see Problem 1). The same effect can be created, to some degree, by a rough surface that can be viewed as a superposition of many gratings with different periodicities.

10.3 Reflection Anisotropy Spectroscopy (RAS)

The technique of Reflection Anisotropy Spectroscopy (RAS) allows surface-sensitive optical spectroscopy despite the large penetration depth of light. This surface sensitivity is achieved by the following symmetry-based trick: The optical response of a solid is dictated by its complex dielectric tensor ϵ or by the complex refraction tensor N. In the case of crystals with an inversion centre, such as a cubic crystal, the tensor is reduced to a complex scalar and we have only addressed this situation so far. Consequently the normal-incidence reflectivity of a cubic crystal should not depend on the azimuthal orientation of the polarisation vector. This is only true, however, for the dielectric response of the bulk crystal; at the surface the inversion symmetry is broken. Any azimuthal anisotropy in the normal-incidence reflectivity of cubic crystals must therefore

have its origin in the surface region.
In a RAS experiment (see Fig. 10.4) one probes the difference in the (almost) normal-incidence reflectivity along two mutually perpendicular orientations of the polarisation vector. Usually one or both of these directions coincide with the principal crystallographic directions in the surface. In Fig. 10.4, the incoming beam is linearly polarised and the polarisation vector lies between two high-symmetry directions on the surface. Here an fcc(110) surface is used and the directions are [001] and $[1\bar{1}0]$, i.e. perpendicular and parallel to the closed-packed rows, respectively. If the surface reflectance is different along these directions, the polarisation for the reflected light is rotated, and this is analysed. Technically, this could be done by a single rotating polariser but here it is done in combination with a photoelastic modulator.

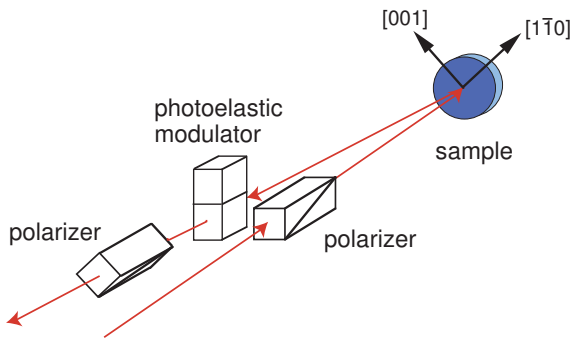

Figure 10.4: Setup for a RAS experiment. The difference in reflectance along two mutually perpendicular directions is measured. After Ref. [82].

This technique is of course rather restricted: the only possible measuring geometry is normal incidence, the bulk crystal has to have inversion symmetry and the surface must be chosen such that it has two mutually perpendicular directions that are not symmetry-equivalent (i.e. fcc(110) works but fcc(001) does not).
One example for the usefulness of RAS is the study of surface states on metal surfaces. Fig. 10.5 shows the electronic structure in the vicinity of the $\bar{Y}$ point of the surface Brillouin zone on Ag(110). Two surface states are found in the projected band gap. One state above and one state below the Fermi level. Fig. 10.6 shows ARPES and RAS spectra for the clean and oxygen-covered Ag(110) surface. The ARPES spectrum taken at the $\bar{Y}$ point shows the surface state right below the Fermi level. Upon oxygen adsorption, this surface state is quenched and a strong oxygen-induced peak is observable at a binding energy of $\approx$1.6 eV. In the RAS spectrum of the clean surface, a pronounced peak is visible at a photon energy of $\approx$1.7 eV. This energy corresponds to an interband

Bibliography

[1] Lars Petersen, private communication.

[2] N. D. Lang and W. Kohn. Theory of metal surfaces: Charge density and surface energy. *Physical Review B*, **1**, 4555, 1970.

[3] Andrea Marini, Giovanni Onida, and Rodolfo Del Sole. Quasiparticle Electronic Structure of Copper in the GW Approximation. *Phys. Rev. Lett.*, **88**, 016403, 2001.

[4] Armando Euceda, D. M. Bylander, and Leonard Kleinman. Self-consistent electronic structure of 6- and 18-layer Cu(111) films. *Phys. Rev. B*, **28**, 528, 1983.

[5] A. Zangwill. *Physics at Surfaces*. Cambridge University Press, 1988.

[6] H. Ibach and D. L. Mills. *Electron Energy Loss Spectroscopy and Surface Vibrations*. Academic Press, 1982.

[7] This suggests that the work function of the sample would have to be known in order to perform the transformation from kinetic energy to binding energy. This, however, is not the case. When performing the transformation, it is only necessary to know the work function of the electron analyser, not that of the sample. This point shall not be discussed further here.

[8] J. J. Yeh and I. Lindau. Atomic subshell photoinoization cross sections and asymmetry parameters: $1 \leq Z \leq 103$. *Atomic Data and Nuclear Data Tables*, **32**, 1, 1985.

[9] David A. Shirley. ESCA. *Advances in Chemical Physics*, **23**, 85, 1973.

[10] Alessandro Baraldi, Silvano Lizzit, Giovanni Comelli, Andrea Goldoni, Philip Hofmann, and Giorgio Paolucci. Core-level subsurface shifted component in a $4d$ transition metal: Ru$(10\bar{1}0)$. *Phys. Rev. B*, **61**, 4534, 2000.

[11] S. Doniach and M. Sunjic. Many-electron singularity in x-ray photoemission and x-ray line spectra from metals. *Journal of Physics C: Solid State Physics*, **3**, 285, 1970.

[12] http://xdb.lbl.gov/.

[13] J. F. Moulder, W. F. Stickle, P. E. Sobol, and K. D. Bomben. *Handbook of X Ray Photoelectron Spectroscopy: A Reference Book of Standard Spectra for Identification and Interpretation of XPS Data*. Physical Electronics, 1995 (re-issue).

[14] L. E. Davis, N. C. MacDonald, P. W. Palmberg, and G. Riach. *Handbook of Auger Electron Spectroscopy: A Reference Book of Standard Data for Identification and Interpretation of Auger Electron Spectroscopy Data*. Physical Electronics, 1978.

[15] E. Zaremba and W. Kohn. Theory of helium adsorption on simple and noble-metal surfaces. *Phys. Rev. B*, **15**, 1769, 1977.

[16] N. D. Lang and A. R. Williams. Theory of atomic chemisorption on simple metals. *Phys. Rev. B*, **18**, 616, 1978.

[17] E. Wimmer, C. L. Fu, and A. J. Freeman. Catalytic promotion and poisoning - all-electron local-density-functional theory of CO on Ni(001) surfaces coadsorbed with K or S. *Physical Review Letters*, **55**, 2618, 1985.

[18] D. A. King and M. G. Wells. Reaction Mechanism in Chemisorption Kinetics: Nitrogen on the (100) Plane of Tungsten. *Proc. Roy. Soc. London A*, **339**, 245, 1974.

[19] A. Baraldi, S. Lizzit, G. Comelli, M. Kiskinova, R. Rosei, K. Honkala, and J. K. Nørskov. Spectroscopic Link between Adsorption Site Occupation and Local Surface Chemical Reactivity. *Phys. Rev. Lett.*, **93**, 046101, 2004.

[20] P. W. Tamm and L. D. Schmidt. Binding States of Hydrogen on Tungsten. *The Journal of Chemical Physics*, **54**, 4775, 1971.

[21] W. A. Brown, R. Kose, and D. A. King. Femtomole Adsorption Calorimetry on Single-Crystal Surfaces. *Chemical Reviews*, **98**, 797, 1998.

[22] R. Smoluchowski. Anisotropy of the Electronic Work Function of Metals. *Phys. Rev.*, **60**, 661, 1941.

[23] M W Finnis and V Heine. Theory of lattice contraction at aluminium surfaces. *Journal of Physics F: Metal Physics*, **4**, L37, 1974.

[24] K. Christmann, G. Ertl, and O. Schober. LEED intensities from clean and hydrogen covered Ni(100) and Pd(111) surfaces. *Surface Science*, **40**, 61, 10 1973.

[25] J. Burchhardt, M. M. Nielsen, D. L. Adams, E. Lundgren, and J. N. Andersen. Structure of Al(111)-($\sqrt{3} \times \sqrt{3}$)-Na: A LEED study. *Phys. Rev. B*, **50**, 4718, 1994.

[26] Ph. Hofmann, K. Pohl, R. Stumpf, and E. W. Plummer. Geometric structure of Be($10\bar{1}0$). *Physical Review B*, **53**, 13715, May 1996.

[27] C. Stampfl, M. Scheffler, H. Over, J. Burchhard, M. Nielsen, D. L. Adams, and W. Moritz, W. Identification of stable and metastable adsorption sites of K adsorbed

on Al(111). *Physical Review Letters*, **69**, 1532, 1992.
[28] S. R. Parkin, H. C. Zeng, M. Y. Zhou, and K. A. R. Mitchell. Low-energy electron-diffraction crystallographic determination for the Cu(110)2x1-O surface-structure. *Physical Review B*, **41**, 5432, 1990.
[29] Alpha T N'Diaye, Johann Coraux, Tim N Plasa, Carsten Busse, and Thomas Michely. Structure of epitaxial graphene on Ir(111). *New Journal of Physics*, **10**, 043033, 2008.
[30] K. Takayanagi, Y. Tanishiro, S. Takahashi, and M. Takahashi. Structure-analysis of Si(111)-(7x7) reconstructed surface by transmission electron-diffraction. *Surface Science*, **164**, 367, 1985.
[31] National Synchrotron Light Source, Brookhaven National Laboratory, EXAFS standards,.
[32] M. Polčik, L. Wilde, and J. Haase. SO_2-induced surface reconstruction of Cu(111): An x-ray-absorption fine-structure study. *Phys. Rev. B*, **57**, 1868, 1998.
[33] F. Song, J. W. Wells, K. Handrup, Z. S. Li, S. N. Bao, K. Schulte, M. Ahola-Tuomi, L. C. Mayor, J. C. Swarbrick, E. W. Perkins, L. Gammelgaard, and Ph. Hofmann. Direct measurement of electrical conductance through a self-assembled molecular layer. *Nature Nanotechnology*, **4**, 373, 2009.
[34] D. A. Wesner, F. P. Coenen, and H. P. Bonzel. Amplitude anisotropy of the bending vibration of CO adsorbed on Ni(110). *Surface Science*, **199**, L419, 1988.
[35] K.-U. Weiss, R. Dippel, K.-M. Schindler, P. Gardner, V. Fritzsche, A. M. Bradshaw, A. L. D. Kilcoyne, and D. P. Woodruff. Chemical shift photoelectron diffraction from molecular adsorbates. *Phys. Rev. Lett.*, **69**, 3196, 1992.
[36] J. Tersoff and D. R. Hamann. Theory of the scanning tunneling microscope. *Phys. Rev. B*, **31**, 805, 1985.
[37] A. Tuxen. *Atomic-scale investigaton of MoS_2-based hydrotreating model catalysts*. Ph.D.-thesis, University of Aarhus, 2011.
[38] C. Klink, L. Olesen, F. Besenbacher, I. Stensgaard, E. Laegsgaard, and N. D. Lang. Interaction of C with Ni(100): Atom-resolved studies of the "clock" reconstruction. *Phys. Rev. Lett.*, **71**, 4350, 1993.
[39] Søren Ulstrup, private communication.
[40] Erik Lægsgaard, private communication.
[41] F. Besenbacher. Scanning tunnelling microscopy studies of metal surfaces. *Reports on Progress in Physics*, **59**, 1737, 1996.
[42] Federico Rosei, private communication.
[43] R. M. Tromp, R. J. Hamers, and J. E. Demuth. Atomic and electronic contributions

to Si(111)-(7x7) scanning-tunneling-microscopy images. *Physical Review B*, **34**, 1388, 1986.

[44] A. W. Munz, C. Ziegler, and W. Gopel. Atomically resolved scanning tunneling spectroscopy on Si(001)-(2x1) asymmetric dimers. *Physical Review Letters*, **74**, 2244, 1995.

[45] Franz J. Giessibl. Advances in atomic force microscopy. *Rev. Mod. Phys.*, **75**, 949, 2003.

[46] G. H. Enevoldsen. *Scanning Probe Microscopy Studies of a Metal Oxide surface*. Ph.D.-thesis, University of Aarhus, 2007.

[47] K Besocke, B Krahl-Urban, and H Wagner. Dipole moments associated with edge atoms; A comparative study on stepped Pt, Au and W surfaces. *Surface Science*, **68**, 39, 11 1977.

[48] R. Błaszczyszyn, M. Błaszczyszyn, and R. Męclewski. Work function of the adsorption system of potassium on tungsten. *Surface Science*, **51**, 396, 1975.

[49] H. J. Levinson, F. Greuter, and E. W. Plummer. Experimental bandstructure of aluminium. *Physical Review B*, **27**, 727, 1983.

[50] E. V. Chulkov and V. M. Silkin. Electronic structure of the Al(001) surface with adsorbed Na halfmonolayer. *Surface Science*, **215**, 385, 1989.

[51] E. W. Plummer and T. Gustafsson. Geometry of Adsorbates on Solid Surfaces. *Science*, **198**, 165, 1977.

[52] E. W. Plummer and W. Eberhardt. Angle-resolved photoemission as a tool for the study of surfaces. *Advances in Chemical Physics*, **49**, 533, 1982.

[53] M. Fuglsang Jensen, T. K. Kim, S. Bengio, I. Yu. Sklyadneva, A. Leonardo, S. V. Eremeev, E. V. Chulkov, and Ph. Hofmann. Thermally induced defects and the lifetime of electronic surface states. *Physical Review B*, **75**, 153404, 2007.

[54] Ph. Hofmann, Ch. Søndergaard, S. Agergaard, S. V. Hoffmann, J. E. Gayone, G. Zampieri, S. Lizzit, and A. Baraldi. Unexpected surface sensitivity at high energies in angle-resolved photoemission. *Physical Review B*, **66**, 245422, 2002.

[55] S. LaShell, B. A. McDougall, and E. Jensen. Spin splitting of an Au(111) surface state band observed with angle resolved photoelectron spectroscopy. *Physical Review Letters*, **77**, 3419, 1996.

[56] A. Tamai, W. Meevasana, P. D. C. King, C. W. Nicholson, A. de la Torre, E. Rozbicki, and F. Baumberger. Spin-orbit splitting of the Shockley surface state on Cu(111). *Phys. Rev. B*, **87**, 075113, Feb 2013.

[57] I. A. Nechaev, M. F. Jensen, E. D. L. Rienks, V. M. Silkin, P. M. Echenique, E. V. Chulkov, and Ph. Hofmann. Hole dynamics in a two-dimensional spin-orbit coupled

electron system: Theoretical and experimental study of the Au(111) surface state. *Physical Review B*, **80**, 113402, 2009.

[58] D. Purdie, M. Hengsberger, M. Garnier, and Y. Baer. An outlook for high-resolution UV photoelectron spectroscopy of solids at low temperature. *Surface Science*, **407**, L671, 1998.

[59] R. J. Smith, J. Anderson, and G. J. Lapeyre. Adsorbate Orientation Using Angel-Resolved Polarization-Dependent Photoemission. *Phys. Rev. Lett.*, **37**, 1081, 1976.

[60] F. Greuter, D. Heskett, E. W. Plummer, and H. J. Freund. Chemisorption of CO on Co(0001). Structure and electronic properties. *Phys. Rev. B*, **27**, 7117, 1983.

[61] I. Pletikosic, M. Kralj, P. Pervan, R. Brako, J. Coraux, A. T. N'Diaye, C. Busse, and T. Michely. Dirac Cones and Minigaps for Graphene on Ir(111). *Physical Review Letters*, **102**, 056808, 2009.

[62] Rosanna Larciprete, Søren Ulstrup, Paolo Lacovig, Matteo Dalmiglio, Marco Bianchi, Federico Mazzola, Liv Hornekær, Fabrizio Orlando, Alessandro Baraldi, Philip Hofmann, and Silvano Lizzit. Oxygen Switching of the Epitaxial Graphene–Metal Interaction. *ACS Nano*, **6**, 9551, 2013/01/15 2012.

[63] K. C. Pandey. New π-Bonded Chain Model for Si(111)-(2×1) Surface. *Phys. Rev. Lett.*, **47**, 1913, 1981.

[64] F. J. Himpsel and N. V. Smith. Photoelectron spectroscopy. *Physics Today*, **38**, 60, 1985.

[65] D. J. Chadi. Atomic and Electronic Structures of Reconstructed Si(100) Surfaces. *Phys. Rev. Lett.*, **43**, 43, 1979.

[66] F. G. Allen and G. W. Gobeli. Work Function, Photoelectric Threshold, and Surface States of Atomically Clean Silicon. *Phys. Rev.*, **127**, 150, 1962.

[67] P. D. C. King, T. D. Veal, C. F. McConville, J. Zúñiga Pérez, V. Muñoz Sanjosé, M. Hopkinson, E. D. L. Rienks, M. Fuglsang Jensen, and Ph. Hofmann. Surface Band-Gap Narrowing in Quantized Electron Accumulation Layers. *Phys. Rev. Lett.*, **104**, 256803, 2010.

[68] Jian-Li Mi, Martin Bremholm, Marco Bianchi, Kasper Borup, Simon Johnsen, Martin Søndergaard, Dandan Guan, Richard C. Hatch, Philip Hofmann, and Bo B. Iversen. Phase Separation and Bulk p-n Transition in Single Crystals of Bi_2Te_2Se Topological Insulator. *Advanced Materials*, **25**, 889, 2013.

[69] S. Agergaard, C. Søndergaard, H. Li, M. B. Nielsen, S. V. Hoffmann, Z. Li, and Ph. Hofmann. The effect of reduced dimensionality on a semimetal: The electronic structure of the Bi(110) surface. *New Journal of Physics*, **3**, 15.1, 2001.

[70] R Stedman, Z Amilius, R Pauli, and O Sundin. Phonon spectrum of beryllium at

80K. *Journal of Physics F: Metal Physics*, **6**, 157, 1976.
[71] J. B. Hannon, E. J. Mele, and E. W. Plummer. Phonon dispersion at the Be(0001) surface. *Phys. Rev. B*, **53**, 2090, 1996.
[72] N. V. Richardson and A. M. Bradshaw. The frequencies and amplitudes of CO vibrations at a metal surface from model cluster calculations. *Surface Science*, **88**, 255, 1979.
[73] Ismail, private communication.
[74] W. Ho, R. F. Willis, and E. W. Plummer. Mechanisms for low-energy-electron vibrational excitation of adsorbates: H on W(100). *Phys. Rev. B*, **21**, 4202, 1980.
[75] M. Schulze. PhD thesis, University of Hannover, 1988, adapted from "Oberflächenphysik des Festkörpers" by M. Henzler and W. Göpel, Teubner, 1991.
[76] S. Lehwald and H. Ibach. Decomposition of hydrocarbons on flat and stepped Ni(111) surfaces. *Surface Science*, **89**, 425, 1979.
[77] Y. J. Chabal. Surface infrared spectroscopy. *Surface Science Reports*, **8**, 211, 5 1988.
[78] B. E. Hayden, K. Kretzschmar, A. M. Bradshaw, and R. G. Greenler. An infrared study of the adsorption of CO on a stepped platinum surface. *Surface Science*, **149**, 394, 1985.
[79] Anton Tamtögl, private communication.
[80] A. M. Lahee, J. P. Toennies, and Ch. Wöll. Low energy adsorbate vibrational modes observed with inelastic helium atom scattering: CO on Pt(111). *Surface Science*, **177**, 371, 1986.
[81] B. C. Stipe, M. A. Rezaei, and W. Ho. Single-Molecule Vibrational Spectroscopy and Microscopy. *Science*, **280**, 1732, 06 1998.
[82] W. Richter. Optical in situ surface control during MOVPE and MBE growth. *Philosophical Transactions of the Royal Society of London, Series A*, **344**, 453, 1993.
[83] K. Stahrenberg, T. Herrmann, N. Esser, J. Sahm, W. Richter, S. V. Hoffmann, and Ph. Hofmann. Surface-state contribution to the optical anisotropy of Ag(110) surfaces: A reflectance-anisotropy-spectroscopy and photoemission study. *Physical Review B*, **58**, R10207, 1998.
[84] L. E. Urbach, K. L. Percival, J. M. Hicks, E. W. Plummer, and H.-L. Dai. Resonant surface second-harmonic generation: Surface states on Ag(110). *Phys. Rev. B*, **45**, 3769, 1992.

Index